Spline Model: a Hydrostatic / non-hydrostatic Dynamic Core with Space-time Second-order Precision and its Exact Tests

Xuzan Gu,[1] **Zhibin Wang**,[1] **Yinglian Guo**[1]

[1]Institute of Heavy Rain, CMA, Wuhan, China

Corresponding author: Xuzan Gu, guxuzan@163.com

Abstract. We present a new explicit quasi-Lagrangian integration scheme with the three-dimensional cubic spline function transform (transform = fitting + interpolation, referred to as "spline format") on a spherical quasi-uniform longitude-latitude grid. It is a consistent longitude-latitude grid, and to verify its feasibility, accuracy, convergence, and stability of the spline format interpolation scheme for the upstream point on the longitude-latitude grid, which may map a quasi-uniform longitude-latitude grid, a set of ideal, exact test schemes, which are recognized and effective internationally, are adopted. The equilibrium flow test, cross-polar flow test, and Rossby–Haurwitz wave test are used to illustrate the spline scheme uniformity to the linear scheme and to overcome the over-dense grid in the polar region and the non-singularity of the poles. The cross-polar flow test demonstrates that the geostrophic wind crosses the correctly polar area, including the South Pole and North Pole. A non-hydrostatic fully compressible dynamical core is used to complete the density flow test, demonstrating the existence of a time-varying reference atmosphere, and that the spline format can simulate highly nonlinear fine-scale transient flows. It can be compared for the two results of the density flow test between the solution of with spline format and the benchmark reference solution of with linear format. The non-hydrostatic dynamical core in the spline format is adopted: it can be successfully simulated for the flow over an ideal mountain, called "topographic gravity wave test", which demonstrating the bicubic surface terrain and terrain-following height coordinates, time-split integration, and vector discrete decomposition method. These can serve as the foundation for the global, unified spline format, numerical model in future.

1 Introduction

Many countries (i.e., UK, US, Japan, Canada, and China) have developed plans to establish globally/regionally unified grid mesh numerical models with horizontal resolutions of 1-100km. However, the global grid point model's forecast level has yet to outperform the currently widely adopted global spectral model.

The spectral model's mathematical foundation is a two-dimensional spectral (spherical harmonics) expansion, which calculates the horizontal upstream point "analytically", whereas the grid point model generally uses some cubic function interpolation to calculate the upstream point. Such an approach raises a simple question: is it possible for the "cubic function" model to outperform the "spectral" model?

What mathematical function should be used to fit some physical field as an unknown "primitive function"? First, let us look at pure mathematics.

It is known that two-dimensional spectral expansion is only "convergent" and can achieve "optimal" least square error. However, the spectrum has a few mathematical shortcomings: 1) the horizontal vector field of the spectrum is mathematically singular at the poles (i.e., the spectral model does not forecast for the poles); 2) there are spurious peaks in the plane (called "Gibbs phenomenon"); 3) the spectrum is not suitable for the vertical format, fitting neither the upper and lower boundaries nor the side boundaries, and thus is not suitable as the global uniform numerical model; and finally, 4) the spectra calculation effort increases rapidly as resolution increases.

There are two types of cubic function interpolation in mathematics, namely, Hermite "double osculating" cubic spline function and the Lagrangian cubic function.

Cubic spline functions include cubic splines, bicubic surfaces (Fergusion, 1964), and tri cubic cubes, all of which have the following mathematical laws/properties:

(1) Convergence to the primitive function and its first- and second-order derivatives (i.e., **convergence**);

(2) Optimal approximation to the primitive function's second-order derivative (i.e., **optimality**);

(3) Second-order central difference being linear principal part, second-order accuracy difference + integration schemes (i.e., **difference, integrality, accuracy**);

(4) Natural cubic splines with the least amount of total curvature (i.e., **stability**);

(5) With periodic, unequally spaced cubic splines (i.e., **periodicity, point selection**);

(6) With multiple cubic spline mathematical boundaries or concatenating other continuous functions (i.e., **boundary adaptability, concatenation**);

(7) With the cubic spline smoothing function (i.e., **smoothness**), eliminating discontinuous cusps or wraps;

(8) Preserving latitudinal and longitudinal symmetry, as well as polar and equatorial symmetry (i.e., **symmetry, non-singular at poles**).

For local interpolation, the Lagrangian cubic function is used. Bilinear interpolation, for example, refers to the 16-point fit and interpolation on a variable field, which is similar to the value obtained from the interpolation of cubic spline function.

All the mathematical laws and properties of the cubic spline function are referred to as the "spline format," and the spline format is appropriate for developing a globally accepted "grid point" numerical model (called a "spline model"). The spline model has a better mathematical foundation than the spectral model and it may be the best one because of the **optimality** of a mathematical law. Therefore, a global multiple nested spline model should replace a modern popular global spectral model + another mesoscale model in the future.

Because the spline format has line, plane, and volume convergence as well as second-order derivative optimality, the physical fields and their first-order derivatives/slope, second-order derivatives/curvature, and second-order mixed partial derivatives/deflection are fitted so that each physical field (i.e., scalar and vector fields) is second-order derivative. This allows for the upstream point to be computed "analytically." The "convergence" of the spline format implies that if the space-time resolution is high enough, the upstream point can always be obtained; in other words, "the weather is predictable".

Layton (2002) completed a three-time-level Euler integration semi-implicit scheme for the shallow water wave equation in the spline format, and the integration test demonstrated that it is a high-order, accurate, and computationally stable method. In comparison, the spectral method will encounter the Legendre transformation high-order complexity.

In the description of atmospheric motion, the dynamic core of the numerical model (i.e., physical field spatial discretization, and time integration) determines the mathematical properties (including model accuracy), physical conservatism, and computational stability of the model.

A non-hydrostatic and fully compressible dynamic core provides the most realistic description of the atmosphere's strong convection weather system. Daley (1988) discovered that when computing normal mode harmonics for zonal waves with a number greater than 400, the hydrostatic and non-hydrostatic schemes differ significantly, implying that the hydrostatic scheme is not appropriate for describing waves with wavelengths less than 100 km. The fully compressible pressure equation, on the other hand, has 3D divergence, which invariably produces acoustic waves, so "calculating acoustic waves" is the key to forecasting the fully compressible pressure field. Durran and Blossey (2012) argued that the fast "acoustic wave," which is not meteorologically significant, limits the integration step of the explicit temporal difference scheme, and that if the acoustic wave is retained, it is necessary to ensure that the "noise" of the barometric disturbance does not cause computational instability.

Dudhia (1993) created a non-hydrostatic mesoscale numerical model MM5 with multi-physics processes, which was followed by the introduction of a new generation of American numerical model Weather Research and Forecasting Model, both of which used a filter subprogram to filter out fast waves: Acoustic waves combined with small-scale gravity waves.

In non-hydrostatic numerical models, generally, the “reference atmospheric profile” must be introduced, causing the “perturbed” barometric field wave on the “reference atmospheric profile”. A corresponding linear perturbation treatment on the pressure and temperature field must then be performed to deduct the vertical pressure gradient force and the reference atmosphere weight having a static constraint relationship with gravity, so that it becomes a non-hydrostatic perturbation balance. Overall, this should be done to improve the accuracy at which vertical pressure gradient force can be determined.

It is generally accepted that the truncation error of spatial differentiation is much larger than that of temporal difference. Additionally, the quasi-Lagrangian integration scheme not only improves the calculation accuracy of spatial difference, but also bases the time step solely on the difference accuracy of the upstream point, rather than the differential stability. However, when compared to the Euler difference conservation scheme, the theoretical design of the quasi-Lagrangian difference conservation scheme has not been devised yet.

Gu (2011) completed the derivation of the fourth-order space-time residual error with quasi-Lagrangian and Euler equations using Taylor series expansion. This demonstrated that using spline format to find the upstream point path of the quasi-Lagrangian method has the same mathematical basis as using a spline format slope, curvature, and deflection to find the Euler displacement, both the numerical solutions are second-order temporal and spatial accuracy, in addition, 4th-order temporal and spatial accuracy can be obtained, but the cubic spline fitting calculation volume grows exponentially.

In numerical models, quasi-Lagrangian integration schemes are commonly used to describe everything from gravity waves to atmospheric long waves. For example, ① time-split integration scheme (KW scheme): a long step for horizontal displacement and short step for vertical displacement; ② semi-implicit semi-Lagrangian integration scheme (SI-SL scheme). Robert et al. (1985) proposed an integration scheme combining the semi-Lagrangian method for advection terms and the semi-implicit scheme for gravity wave terms, and compared it to the Eulerian integration scheme at the same spatial resolution, where the former time step is taken to be ten times that of the latter, and the calculation results were comparable. The SI-SL integration scheme is thought to be capable of preserving a physical property that can be described as “non-hydrostatic and fully compressible” (Pinty et al. 1995).

The GRAPES (Global/regional assimilation and prediction system) globally/regionally unified (grid point) numerical model, developed in China, uses Lagrangian cubic function “bilinear (local area) interpolation” to calculate the upstream point. This model has a large time step and avoids acoustic waves by using SI-SL integration. However, the large step length causes large dispersion, which results in large truncation errors in the coupling of physical processes, as well as the need to solve the generalized conjugate residual Helmholtz equation of the 3D barometric perturbation, which necessitates a large computational volume. This results in a high-resolution numerical model and a reconsideration of explicit integration schemes.

The horizontal pressure gradient force on the grid point terrain versus terrain-height coordinates has a large relative error. To extend the numerical stability limit over steep slopes, Günther Zängl (2012) developed a truly horizontal pressure-gradient discretization based on the ideas formulated by Mahrer in the 1980s, since the pressure gradient is evaluated in the terrain-following coordinate system, which necessitates a metric correction term that is prone to numerical instability if the height difference between adjacent grid points is larger than the vertical layer spacing. Gu (2013) introduced a second-order derivable bicubic surface terrain, with a constant slope, curvature, and deflection, and established the bicubic surface terrain, and the terrain-following height coordinates, calculated the horizontal barometric pressure gradient force over the bicubic surface terrain with second-order accuracy and inverted the sea level pressure field.

Su et al. (2018) proposed a three-dimensional reference atmosphere for GRAPES_GFS to replace the one-dimensional reference atmosphere, the isothermal atmosphere, in order to reduce the order of magnitude of the model dynamic core nonlinear terms, re-derive the dynamical equations, and verify and improve dynamic core accuracy using the ideal test. Through testing the GRAPES, Liu et al. (2011) concluded that 6×grid spacing is an effective resolution scale for grid point topography.

Cartesian coordinates are appropriate for describing Newtonian motion. When using spherical coordinates to describe atmospheric motion and calculating the motion of a continuous wind field, the 3D wind and displacement fields must be decomposed in unit vectors on spherical coordinates (called "vector discrete," Bates et at. 1990). The traditional vector discretization method involves moving the air parcel from the upstream point to the Euler forecast point in the direction of the unit vector in the middle of the path; this clearly does not treat the wind field as a continuous vector field.

As the core of the numerical model, the dynamic framework needs an effective and referable method to verify the correctness of its scientific scheme and programming. Doing exact test is an effective method and has been recognized and widely applied globally (Yang et al. 2007; Yang et al. 2008; Nunalee et al. 2015; Jacobs et al. 2015; Gavrilov et al. 2015; Li et al. 2022). All newly developed numerical forecast models should go through a similar ideal field test. The design of an ideal test scheme based on the characteristics of a model remains a challenge. The general strategy is to create ideal initial values for a specific reduced physical model or design some model initial values to satisfy specific kinetic constraints, turn off factors that are irrelevant to the process under consideration, and then test the accuracy and stability of the model's dynamic core using ideal field integration tests.

Since different numerical schemes are used for different models, the properties of the model to be validated need to be considered in the design of the ideal field test scheme. The following ideal field tests are created based on the GRAPES model's non-hydrostatic, semi-implicit semi-Lagrangian, and multi-scale properties (Yang et al. 2007), for example: the equilibrium flow test is designed to check the accuracy of the semi-Lagrangian interpolation; the cross-polar flow test to evaluate the model's discrete scheme at the poles; the density flow test to verify the ability of the non-hydrostatic model to simulate fine-scale and transient features, and the 3D topographic wave test to evaluate the model's dynamic framework in simulating the horizontal and vertical propagation of cross-mountain flow gravity waves.

Zuo et al. (2004) designed a global Euler differential grid model "IAP (Institute of Atmospheric Physics, Chinese Academy of Sciences) AGCM-III" with the time integration scheme of an improved nonlinear iterative, the wave phase velocity and pattern, and energy propagation in its dynamic framework are performed by the ideal field of Rossby–haurwitz wave test.

The Rossby–Haurwitz wave ideal test with a T63L17 spectral model "spectral transformation" and integration of 80 d on the Gaussian grid produces an incorrect result of "partial/flat circle", asymmetry concerning the pole in the polar region, and the horizontal vector field at the pole is a mathematical singularity when using the spectral expansion method.

There is an industry-accepted, valid, and comparable set of ideal tests to test the feasibility, consistency, convergence, and accuracy of the non-hydrostatic fully compressible dynamic core.

Fast-wave solutions of atmospheric motion, such as the elastic, acoustic wave solution and the gravity wave solution, are contained in the non-hydrostatic fully compressible dynamic core of the original atmospheric motion equation (Qian, et al. 1998; Benacchio, et al. 2014). The 3D gravity wave test checks the reasonableness and ability of "describing" gravity waves. Smith et al. (1980) successfully modeled and simulated a hydrostatic, non-compressible fluid (called "Boussinesq-approximation") advection over a "bell-shaped" isolated mountain to form a gravity wave flow pattern. They did this by using Fourier analysis to present a linear theory of airflow perturbation and the terrain perturbation test for a steady airflow crossing over an isolated mountain in a stable stratification. The Fourier analytical solution was compared with the simulated numerical solution, and the gravity waves had a vertical propagation structure. The maximum wave amplitude was at the top of the mountain, and it was parabolic with downhill flow propagation and dispersion, forming "high pressure in front of the mountain, low pressure behind the mountain", "dispersed, deflected, convergent", and continuous lee wave flow pattern of advection above, and the lateral horizontal dispersion/convergence airflow attaining equilibrium with sinking /rising, warming /temperature reducing air layers.

The density flow test is the ideal test for verifying the non-hydrostatic model. To compare the consistency, convergence, and precision of the numerical solutions produced by the new format and the conventional monotone format, Straka et al. (1993) introduced a non-hydrostatic, fully compressible dynamic framework simulating nonlinear density flow, reference solutions with various resolutions, namely, benchmark standard solutions, but for the linear format represented by the central difference.

Non-hydrostatic models developed by different countries all use the density flow test and cross-mountain flow gravity wave test as a model dynamic core to simulate the level of nonlinear flow, the results of which are compared with benchmark standard. For instance, the German Lokal model, the UK unified model, the US mesoscale model (Xue et al. 2000), and the Japanese Meteorological Institute NPD-NHM (Saito et al. 1998).

Xu et al. (1996) performed numerical simulations to study the kinematics and dynamics of two-dimensional density currents propagating in a uniformly sheared environmental flow within a vertically confined channel. The physical properties of the numerical solutions relative to those of theoretical predictions and the initial cold pool depth and shear were chosen to be either similar to or significantly different than those prescribed by the theoretical steady-state model. Xue et al. (1997) extended the idealized two-fluid model of a density current in constant shear to the case where the inflow shear is confined to the low levels, in which an analytical solution must be determined by the conservation of mass, momentum, vorticity, and energy.

Yang et al. (2008), for the GRAPES numerical model, completed a non-hydrostatic completely compressible dynamic core density flow test and a 3D gravity wave test. Gavrilov et al. (2015) performed high-resolution numerical simulations of nonlinear acoustic-gravity waves (AGWs) at altitudes 0–500km and compared them with analytical polarization relations of linear AGW theory. Li et al. (2022) develop a numerical model, ISWFoam with a modified k–ω SST model, to simulate internal solitary waves (ISWs) in continuously stratified, incompressible, viscous fluids based on a fully three- dimensional Navier–Stokes equation with the finite-volume method. ISWFoam can accurately simulate the waveform generation and evolution of ISWs, the ISW breaking phenomenon, and the interaction between ISWs and complex topography.

An important difference between the density flow test and the gravity wave test is that the former is a downburst in a very unstable stratification, and the latter is a cross-mountain flow below the stable stratification. To calculate the acoustic wave, all the density flow tests adopted a very short time step (0.1 s), while the gravity wave tests used a longer time step (10 s), then the latter should have a different acoustic wave calculation scheme.

2 Basic numerical model equations

2.1 Atmospheric motion equations

In atmospheric motion equations of "thin atmosphere" on spherical coordinates (longitude, latitude and geopotential height (λ, φ, z), $\lambda \in [0, 2\pi]$, $\varphi \in [-\frac{\pi}{2}, \frac{\pi}{2}]$, distance from air parcel to the geo center $r = r_e + z$, mean radius of the Earth r_e, $(\partial x, \partial y, \partial z) \hat{=} (r\cos\varphi\partial\lambda, r\partial\varphi, \partial r)$, assume frictionless, water vapor-free, and water vapor source–sink, time as t, air pressure as p, air temperature as T, specific humidity as q, 3D wind field $V = (u, v, w)$, $f = 2\Omega\sin\varphi$, $\tilde{f} = 2\Omega\cos\varphi$, spin velocity of the Earth Ω and the gravitational constant as g, the air to gas constant R and the constant pressure specific heat as $\mathrm{C_p}$, and $\kappa = \mathrm{R/C_p}$, "$\hat{=}$" is the defined symbol):

$$\frac{du}{dt} = -\mathrm{R}T\frac{\partial \ln p}{\partial x} + fv - \tilde{f}w + \frac{uv \cdot \tan\varphi - uw}{r_e} \hat{=} a_u \tag{1}$$

$$\frac{dv}{dt} = -\mathrm{R}T\frac{\partial \ln p}{\partial y} - fu - \frac{u^2 \tan\varphi + vw}{r_e} \hat{=} a_v \tag{2}$$

$$\frac{dw}{dt} = -\mathrm{R}T\frac{\partial \ln p}{\partial z} - g + \tilde{f}u + \frac{u^2 + v^2}{r_e} \hat{=} a_w \tag{3}$$

$$\frac{d\ln p}{dt} = \frac{-1}{1-\kappa}\nabla \cdot \mathbf{V} \hat{=} a_p \tag{4}$$

$$\frac{d\ln T}{dt} = \frac{-\kappa}{1-\kappa}\nabla \cdot \mathbf{V} \hat{=} a_T (= \kappa a_p) \tag{5}$$

$$q = \frac{dq}{dt} \equiv 0 \tag{6}$$

Let $P \hat{=} (p, T, q, u, v, w)$, the first-order derivative (1st-order variability) of P is known to be $\frac{dP}{dt} \hat{=} a$, and (1-3) equation (a_u, a_v, a_w) is the generalized Newtonian force per unit mass of air: the three components of the combined force of "barometric gradient force + gravity + Coriolis force + curvature force"; (4-5) equation (a_p, a_T) is the 3D dispersion adiabatic variability of the pressure and temperature field; and equation q is the water vapor source–sink and phase variability, which is zero during dry adiabatic process.

Because *u* and the *u*-equation are not defined at the poles, while *v* and the *v*-equation are defined at the poles. In the north and south poles (denoted by subscripts *N* and *S*), define the parallel components of 0°E $(\lambda = 0)u$ as u_N and u_S, and of 0°E v as v_N and v_S, respectively, and for (u_N, v_N) and (u_S, v_S), (or any horizontal vector), the following trigonometric function vector decomposition can be performed:

$$u_{N(\lambda)} = u_N \cos\lambda + v_N \sin\lambda\,;\;\; v_{N(\lambda)} = v_N \cos\lambda - u_N \sin\lambda$$

$$u_{S(\lambda)} = u_S \cos\lambda - v_S \sin\lambda\,;\;\; v_{S(\lambda)} = v_S \cos\lambda + u_S \sin\lambda \qquad (7)$$

and with $u_N \triangleq u_{N(0)} \equiv v_{N(3\pi/2)}$ and $u_S \triangleq u_{S(0)} \equiv v_{S(\pi/2)}$, similarly, then, horizontal baric gradients are: $(\frac{\partial \ln p}{\partial x})_N \equiv (\frac{\partial \ln p}{\partial y})_{N(3\pi/2)}$ and $(\frac{\partial \ln p}{\partial x})_S \equiv (\frac{\partial \ln p}{\partial y})_{S(\pi/2)}$.

The v_N-equation and the v_S-equation can be derived by taking $\varphi \to \pm\frac{\pi}{2}$ in the *v*-equation (equation (2)), where: $\lim\limits_{\varphi\to\pm\frac{\pi}{2}} u^2 \tan\varphi = \lim\limits_{\varphi\to\pm\frac{\pi}{2}} (\frac{r_0 \cos\varphi \,\mathrm{d}\lambda}{\mathrm{d}t})^2 \tan\varphi = \lim\limits_{\varphi\to\pm\frac{\pi}{2}} r_0^2 (\frac{d\lambda}{dt})^2 \cos\varphi \sin\varphi = 0$ (high-order infinitesimal), whereas the u_N-equation and the u_S-equation are derived by rotating the v_N-equation and the v_S-equation clockwise along the Earth's axis by 90º, respectively, with:

$$\frac{du_N}{dt} = -\mathrm{R}T(\frac{\partial \ln p}{\partial y})_{N(3\pi/2)} + fv_N - \frac{u_N w}{r_e} \triangleq a_{u_N} \qquad (8)$$

$$\frac{du_S}{dt} = -\mathrm{R}T(\frac{\partial \ln p}{\partial y})_{S(\pi/2)} + fv_S - \frac{u_S w}{r_e} \triangleq a_{u_S} \qquad (9)$$

$$\frac{dv_N}{dt} = -\mathrm{R}T(\frac{\partial \ln p}{\partial y})_{N(0)} - fu_N - \frac{v_N w}{r_e} \triangleq a_{v_N} \qquad (10)$$

$$\frac{dv_S}{dt} = -\mathrm{R}T(\frac{\partial \ln p}{\partial y})_{S(0)} - fu_S - \frac{v_S w}{r_e} \triangleq a_{v_S} \qquad (11)$$

2.2 Terrain-following vertical coordinates and horizontal pressure gradient calculation

Transforming the height (*z*) coordinate in atmospheric motion equations (equations (1–6)) to terrain-following height ($\hat{z}$) coordinate, the model introduces a second-order derivable "steady slope, curvature, and deflection" bicubic surface terrain, and defines the terrain-following vertical coordinates (called "$\hat{z}$ coordinates", the bottom and top layers of the model are denoted by subscripts s and T, respectively, and let the terrain height be z_s, the top layer height be z_T, z_T isa constant, and $\Delta Z_s = z_T - z_s$):

$$\hat{z} = \frac{z - z_s}{z_T - z_s} z_T = \frac{z - z_s}{\Delta Z_s} z_T\,,\;\; z = \frac{\Delta Z_s}{z_T}\hat{z} + z_s \;(0 \le \hat{z} \le z_T) \qquad (12)$$

The vertical velocity ($\hat{w}$) in $\hat{z}$ coordinates can be calculated as follows:

$$\hat{w} \triangleq \frac{d\hat{z}}{dt} = \frac{z_T}{\Delta Z_s} w - \frac{\Delta Z_{\hat{z}}}{\Delta Z_s} w_s \tag{13}$$

In the above equation, $w_s \triangleq w_s(x, y, \hat{z}) = u \cdot z_s^x + v \cdot z_s^y$ and (z_s^x, z_s^y) are the terrain slopes, and w_s is known as the "terrain forced uplift speed".

According to (8), there is a one-to-one diagnostic relationship between $\hat{w}$ and (u, v, w), at the ground level ($\hat{z} = 0$) $\hat{w}_s \equiv 0$ and at the top level ($\hat{z} = z_T$) $\hat{w}_T \equiv 0$.

From the z-coordinate to the $\hat{z}$ -coordinate, through vertical derivative transformation ($\frac{\partial \hat{z}}{\partial z} = \frac{z_T}{\Delta Z_s}$), the equation of static equilibrium is:

$$\frac{\partial \ln p}{\partial \hat{z}} = -\frac{\Delta Z_s}{z_T} \frac{\mathrm{g}}{\mathrm{R}T} \tag{14}$$

Through the horizontal derivative transformation, the horizontal barometric pressure gradient is decomposed into the $\hat{z}$ -coordinate horizontal barometric pressure gradient, and the terrain slope barometric pressure difference (suppose $\Delta Z_{\hat{z}} = z_T - \hat{z}$):

$$(\frac{\partial \ln p}{\partial x})_z = (\frac{\partial \ln p}{\partial x})_{\hat{z}} - \frac{\Delta Z_{\hat{z}}}{\Delta Z_s} \frac{\partial \ln p}{\partial \hat{z}} z_s^x \ , \ (\frac{\partial \ln p}{\partial y})_z = (\frac{\partial \ln p}{\partial y})_{\hat{z}} - \frac{\Delta Z_{\hat{z}}}{\Delta Z_s} \frac{\partial \ln p}{\partial \hat{z}} z_s^y \tag{15}$$

The horizontal pressure gradient force in $\hat{z}$ coordinates is calculated using the above equation.

In addition, the three-dimensional divergence in $\hat{z}$ coordinates is calculated as follows:

$$\nabla \cdot \mathbf{V} = (\frac{\partial u}{\partial x} + \frac{\partial v}{\partial y})_{\hat{z}} + \frac{\partial \hat{w}}{\partial \hat{z}} - \frac{v \tan\varphi}{r_e} - \frac{w_s}{\Delta Z_s} \tag{16}$$

2.3 Time-varying reference atmosphere and vertical pressure gradient calculation

For simplicity, only the *z*-coordinate is described.

We can derive the time-varying / 4-dimensional reference atmosphere $\bar{p}(t, x, y, z)$ from the *w*-equation ((3)) and suppose $a_w \equiv 0$, it satisfies the following complete "static equilibrium equation":

$$\frac{\partial \ln \bar{p}}{\partial z} = -\frac{\bar{g}}{\mathrm{R}T} \tag{17}$$

The above equation $\bar{g} = g - \tilde{f}u - \frac{u^2 + v^2}{r} \approx g$, shows that the time-varying reference atmosphere is a function of the air column's "temperature, humidity (R), wind (weightlessness: $-(u^2 + v^2)/r$), and

Coriolis force ($-\tilde{f}u$) and gravity (g may not be a constant)," and if we take $\bar{g} \equiv g$, then $\bar{p}$ is only determined by the temperature, humidity and constant gravity fields in the model atmosphere.

The altitude difference integration is then performed for equation (17), using the top layer $p_{\mathrm{T}} \equiv \bar{p}_{\mathrm{T}}$ as a constant, we can find $\bar{p}$, and $\bar{p}$ is "each layer 'static force' weight".

Then suppose $p = \bar{p} \cdot p'$, $\dfrac{\partial \ln p'}{\partial z}$ can be found, then the vertical pressure gradient and vertical pressure gradient force and vertical acceleration (a_w) calculated as follows:

$$\frac{\partial \ln p}{\partial z} = \frac{\partial \ln \bar{p}}{\partial z} + \frac{\partial \ln p'}{\partial z} = \frac{\partial \ln p'}{\partial z} - \frac{\bar{g}}{\mathrm{R}T} \tag{18}$$

$$a_w = -\mathrm{R}T \frac{\partial \ln p'}{\partial z} \tag{19}$$

When altitude difference integration is used for the static equilibrium equation, the static pressure field-time-varying reference atmosphere is separated from the non-static pressure field, allowing the vertical pressure gradient force and displacement to be calculated accurately without the use of the atmospheric reference profile.

2.4 Hydrostatic vertical displacement calculation

Let, in layers, the model coordinate height be Z, and for the gravity balance equation (17), the static geopotential height of each layer can be found through pressure difference ($p_s \to p$) integration from the bottom of the model upwards:

$$z = z_s + \int_p^{p_s} \frac{\mathrm{R}T}{g} \mathrm{d} \ln p \tag{20}$$

Using equation (20), the vertical displacement $\Delta z = z - \mathrm{Z}$ and vertical velocity $w = \Delta z / \Delta t$ after hydrostatic horizontal advection of each layer in one Δt are calculated.

2.5 Hydrostatic and non-hydrostatic divergence separation

The hydrostatic continuity equation (the "pressure coordinate" continuity equation, denoted by the subscript $_{\mathrm{p}}$, and defining the air pressure variability $\omega \hat{=} \dfrac{dp}{dt}$, is given directly for simplicity (without the derivation) as:

$$\frac{\partial \omega}{\partial p} + \left(\frac{\partial u}{\partial x} + \frac{\partial v}{\partial y}\right)_p - \frac{v \tan \varphi}{r} = 0 \tag{21}$$

The $\hat{z}$ coordinate hydrostatic continuity equation (assuming the "coordinate transformation term") is obtained by mathematical transforming the equation (21) from pressure coordinates to $\hat{z}$ coordinates:

$(\frac{\partial u}{\partial x})_{\hat{z}} = (\frac{\partial u}{\partial x})_p + \frac{\partial u}{\partial p}(\frac{\partial p}{\partial x})_{\hat{z}}$, $(\frac{\partial v}{\partial y})_{\hat{z}} = (\frac{\partial v}{\partial y})_p + \frac{\partial v}{\partial p}(\frac{\partial p}{\partial y})_{\hat{z}}$; substituting into the equation (21), it is obtained that $D_{\hat{z}} \mathrel{\hat{=}} \frac{\partial u}{\partial p}(\frac{\partial p}{\partial x})_{\hat{z}} + \frac{\partial v}{\partial p}(\frac{\partial p}{\partial y})_{\hat{z}}$):

$$\frac{\partial \omega}{\partial p} + (\frac{\partial u}{\partial x} + \frac{\partial v}{\partial y})_{\hat{z}} - \frac{v \tan\varphi}{r} - D_{\hat{z}} = 0 \qquad (22)$$

In equation (22), the hydrostatic horizontal divergence is defined as follows: $D_{sta} \mathrel{\hat{=}} (\frac{\partial u}{\partial x} + \frac{\partial v}{\partial y})_{\hat{z}} - \frac{v \tan\varphi}{r} - D_{\hat{z}}$:

$$\frac{\partial \omega}{\partial p} = -D_{sta} \qquad (23)$$

The 3D divergence (Equation (16)) can be divided into two parts: the hydrostatic horizontal divergence term (D_{sta}) and the non-hydrostatic vertical divergence term (D_{ins}, $D_{\mathrm{ins}} \mathrel{\hat{=}} \frac{\partial \hat{w}}{\partial \hat{z}} - \frac{w_s}{\Delta Z_s} + D_{\hat{z}}$), yielding: $\nabla \cdot \mathbf{V} = D_{sta} + D_{ins}$.

We can find the air pressure variability of each layer by integrating the vertical pressure difference of equation (23), which is used to forecast the hydrostatic pressure and temperature field of each layer.

As a result of the preceding formulation, the 3D divergence $\nabla \cdot \mathbf{V}$ can directly act on the "fully compressible" gas block (so called "air parcel"), resulting in pressure and temperature increments for the adiabatic air parcel. When the divergence field is divided into hydrostatic and non-hydrostatic components, where the D_{sta} term represents the "hydrostatic mass" acting / adding on each layer of the air parcel after the integration of the vertical pressure difference, the air parcel can be used to obtained the "hydrostatic" pressure and temperature increments; meanwhile, the non-hydrostatic process can be treated as an oscillation superimposed on the "hydrostatic equilibrium" pressure-temperature field during the time integration process, which derives from the term D_{ins}, i.e., from the topographic uplift term $\frac{w_s}{\Delta Z_s}$, and is accompanied by the vertical divergence term $\frac{\partial \hat{w}}{\partial \hat{z}}$ ($\frac{\partial \hat{w}}{\partial \hat{z}}$ also generates compressional waves - acoustic waves), note that D_{sta} and D_{ins} have coordinate transformation term with the opposite symbol $D_{\hat{z}}$, but the former requires vertical pressure difference integration before acting on the air parcel, whereas the latter acts directly on the air parcel. And in the gravity wave test in this study, we showed that $D_{\hat{z}}$ is a small magnitude term.

The above derivative “hydrostatic continuity equation” shows that under the assumption of static equilibrium, the term D_{ins} disappears (canceled in the process of deriving the “hydrostatic continuity equation”), and its physical significance is: the topographic lift term $\frac{w_s}{\Delta Z_s}$ acts on the air column first, and then the column tend to be in hydrostatic equilibrium (vertical acceleration $a_w \to 0$); and the $\frac{\partial \hat{w}}{\partial \hat{z}}$ term is the oscillation on the hydrostatic equilibrium, during which the oscillation “fast wave” tends to flatten out (when the air column reaches hydrostatic equilibrium $a_w = 0$).

As a physical concept, the “non-hydrostatic process” can be defined here: the oscillations of each layer of the column under the action of the non-hydrostatic D_{ins} term, actually under the action of the pressure gradient force a_w, can be flattened out in one-time step Δt. The physical “single pendulum” of each layer moves consistently from a position deviating from the hydrostatic equilibrium $a_w \neq 0$ to the hydrostatic equilibrium position $a_w = 0$ (hereinafter called “half-wave oscillation”), then “half-wave oscillation” can avoid the instability of the oscillation. Sound waves, for example, can have n oscillations in one-time step, whereas the “half-wave oscillation” only allows it to stay at the “hydrostatic equilibrium” position until $D_{\mathrm{ins}} = 0$.

The preceding derivation demonstrates that the physical basis of the quasi-Lagrangian “time-split” integration scheme is the separation of hydrostatic and non-hydrostatic three-dimensional divergence. Specifically, short steps are used to forecast non-hydrostatic fully compressible vertical convection and pressure and temperature fields, while long steps are used to forecast hydrostatic horizontal advection and pressure and temperature fields.

3 Quasi-Lagrangian forecast equation

3.1 Quasi-Lagrangian forecast equation with space-time second-order accuracy

Given a time step Δt, forecast variable $P(t+\Delta t, x, y, z)$, and a 2nd-order variability of P $\frac{\mathrm{d}^2 P}{\mathrm{d}t^2} = \frac{\mathrm{d}a}{\mathrm{d}t} \triangleq a^{(2)}$, we can generalize the 2nd-order variability quasi-Lagrangian forecast equation as:

$$
\begin{aligned}
P(t+\Delta t, x, y, z) &= P(t, x-\Delta x, y-\Delta y, z-\Delta z) + \\
&\quad + a(t, x-\Delta x, y-\Delta y, z-\Delta z)\Delta t + \\
&\quad + a^{(2)}(t, x-\Delta x, y-\Delta y, z-\Delta z)\frac{\Delta t^2}{2}
\end{aligned} \tag{24}
$$

Assume 3D upstream point $\dddot{P} \triangleq P(t, x-\Delta x, y-\Delta y, z-\Delta z)$, with Taylor series 2nd order spatial residual taken for $\dddot{P}$ (similar with $\ddot{a}$ and $\ddot{a}^{(2)}$):

$$\dddot{P} \approx P(t,x,y,z) - \Delta x\frac{\partial P}{\partial x} - \Delta y\frac{\partial P}{\partial y} - \Delta z\frac{\partial P}{\partial z} +$$

$$+\frac{\Delta^2 x}{2}\frac{\partial^2 P}{\partial x^2} + \frac{\Delta^2 y}{2}\frac{\partial^2 P}{\partial y^2} + \frac{\Delta^2 z}{2}\frac{\partial^2 P}{\partial z^2} +$$

$$+\Delta x\Delta y\frac{\partial^2 P}{\partial x\partial y} + \Delta x\Delta z\frac{\partial^2 P}{\partial x\partial z} + \Delta y\Delta z\frac{\partial^2 P}{\partial y\partial z} \qquad (25)$$

If the high-order minima $\frac{\partial^2 P}{\partial x\partial z}$ and $\frac{\partial^2 P}{\partial y\partial z}$ are omitted ($\frac{\partial^2 P}{\partial x\partial y}$ kept), for "thin atmosphere," the above equation becomes:

$$\dddot{P} \approx P(t,x,y,z) - \Delta x\frac{\partial P}{\partial x} - \Delta y\frac{\partial P}{\partial y} - \Delta z\frac{\partial P}{\partial z} +$$

$$+\frac{\Delta^2 x}{2}\frac{\partial^2 P}{\partial x^2} + \frac{\Delta^2 y}{2}\frac{\partial^2 P}{\partial y^2} + \frac{\Delta^2 z}{2}\frac{\partial^2 P}{\partial z^2} + \Delta x\Delta y\frac{\partial^2 P}{\partial x\partial y}$$

$$\approx \ddot{P} - \Delta z\frac{\partial P}{\partial z} + \frac{\Delta z^2}{2}\frac{\partial^2 P}{\partial z^2} \qquad (26)$$

The horizontal, two-dimensional upstream point in the preceding equation, $\ddot{P} \triangleq P(t, x-\Delta x, y-\Delta y, z)$.

3.2 Space-time second-order accuracy forecast equation in spline format

The mathematical laws of convergence, optimality, periodicity, and boundary adaptability of the second-order derivative "difference + integral" are all present in the spline format. The *P*-field "line, surface, and volume" become second-order derivable by fitting the cubic spline function of the variable (*P*) field to obtain the slope P^x, P^y, P^z, curvature P^{xx}, P^{yy}, P^{zz}, and deflection P^{xy}, P^{xz}, P^{yz} (obtained from the orthogonal cubic spline). The "spline format" entails considering the following derivatives: $\frac{\partial P}{\partial x} \approx P^x$, $\frac{\partial P}{\partial y} \approx P^y$, $\frac{\partial P}{\partial z} \approx P^z$, $\frac{\partial^2 P}{\partial x^2} \approx P^{xx}$, $\frac{\partial^2 P}{\partial y^2} \approx P^{yy}$, $\frac{\partial^2 P}{\partial z^2} \approx P^{zz}$, $\frac{\partial^2 P}{\partial x\partial y} \approx P^{xy}$, $\frac{\partial^2 P}{\partial x\partial z} \approx P^{xz}$ and $\frac{\partial^2 P}{\partial y\partial z} \approx P^{yz}$, as a result, it is convenient to present the horizontal and vertical pressure gradients and divergence in the spline format.

The 3D motion upstream point in spline format $\dddot{P}$ (as with $\ddot{a}$ and $\ddot{a}^{(2)}$) is as follows:

$$\ddot{P} \approx P(t,x,y,z) - \Delta x P^{x} - \Delta y P^{y} - \Delta z P^{z} +$$

$$+ \frac{\Delta x^2}{2} P^{xx} + \frac{\Delta y^2}{2} P^{yy} + \frac{\Delta z^2}{2} P^{zz} +$$

$$+ \Delta x \Delta y P^{xy} + \Delta x \Delta z P^{xz} + \Delta y \Delta z P^{yz}$$

$$\approx \ddot{P} - \Delta z P^{z} + \frac{\Delta z^2}{2} P^{zz} \tag{27}$$

Therefore, in the "spline format (space-time discretization)" the general forecast equation ((24)) becomes the general second-order accuracy forecast equation.

$$P^{t+\Delta t} \hat{=} P(t+\Delta t, x, y, z) = \ddot{P} + \ddot{a}\Delta t + \ddot{a}^{(2)}\Delta t^2 / 2 \tag{28}$$

The forecast equation above, shows that the upstream point generally follows a nonlinear path, whereas the equations (25-26) are along the "spline format" path in the time period Δt, where the air parcels arrive at the Euler points (x, y, z) with all physical properties and subject to the respective variabilities.

3.3 First-order variability (explicit) and second-order variability (implicit) forecast equations

Because the second-order variability $a^{(2)}$ is generally unknown, if we set $\ddot{a}^{(2)} \equiv 0$ within the time period Δt, that is, the first-order variability $\ddot{a} \equiv c$, c is a constant, then the equation (26) is only the first-order variability "(1 time level) explicit" forecast equation.

$$P^{t+\Delta t} = \ddot{P} + \ddot{a}\Delta t \tag{29}$$

And if we set $\ddot{a}^{(2)} \equiv c \neq 0$, c is a constant, unknown in Δt time period, substituting into equation (25):

$$P^{t+\Delta t} = \ddot{P} + \ddot{a}\Delta t + c\frac{\Delta t^2}{2} \tag{30}$$

Substituting $P \Rightarrow a$ into the above equation and considering the 2nd order variability of P (1st order variability of a) as $\ddot{a}^{(2)} \equiv c$, we get:

$$a^{t+\Delta t} = \ddot{a} + \ddot{a}^{(2)}\Delta t = \ddot{a} + c\Delta t \tag{31}$$

The above equations $\ddot{a}$ and $a^{t+\Delta t}$ represents the first-order variability of the upstream point at the initial and final moments of $t \to t+\Delta t$, and the average second-order variability $c = \dfrac{a^{t+\Delta t} - \ddot{a}}{\Delta t}$ is obtained by substituting into equation (30), and the second-order variability "(2 time layers) implicit" forecast equation is obtained:

$$P^{t+\Delta t} = \ddot{P} + \frac{\ddot{a} + a^{t+\Delta t}}{2}\Delta t \tag{32}$$

Clearly, the second-order variability "implicit" forecast equation has a higher accuracy than the first-order variability "explicit" forecast equation.

The wind field forecast (equations (1–3)) uses the first-order variability forecast equation, whereas the pressure and temperature (humidity) field forecast (equations (4–6)) uses the second-order variability forecast equation, because the pressure and temperature (humidity) field variability is a 3D divergence field implied by the time-step 3D displacement, so it is still an explicit integration scheme.

4 Quasi-Lagrangian time integration scheme

4.1 Calculation of the upstream point

(See Gu, 2011) on a "normal" geographic latitude-longitude grid mesh-orthogonal A-grid, the Coons bicubic surface fit of a variable field can be achieved, and the topological rectangular mesh of an A-grid patch corresponds to Hermite bicubic patches in one-to-one correspondence, with each "patch" consisting of four variable values (P_{00}, P_{01}, P_{10}, P_{11}), eight first-order partial derivatives (P_{00}^{x}, P_{01}^{x}, P_{10}^{x}, P_{11}^{x}, P_{00}^{y}, P_{01}^{y}, P_{10}^{y}, P_{11}^{y}), and four second-order mixed partial derivatives (P_{00}^{xy}, P_{01}^{xy}, P_{10}^{xy}, P_{11}^{xy}). Because the upstream point must fall on an A-grid patch, as a result, the horizontal upstream point ($\ddot{P}$) coordinates and displacement, and variable values can be resolved and calculated.

Simultaneously, the variable field's vertical cubic spline fit is performed to calculate the coordinates, displacements, and variable values of the vertical upstream point ($\dddot{P}$).

In comparison to the traditional linear format, the spline format can be used to calculate horizontal advection motion "slope", bending motion "curvature", and torsional motion "deflection". After fitting all variable scalar and vector fields with "horizontal bicubic surface + vertical cubic spline", each variable field is second-order derivable, and the upstream point can be obtained using the "spatial second-order accuracy" analytical method.

4.2 Wind field forecast

According to Newton's law of motion, to find the "third motion" path-3D displacement of the upstream point and forecast variable values using explicit iterative interpolation, an implicit iteration should be performed to calculate the 3D displacement of the upstream point $(\Delta x, \Delta y, \Delta z) = (\ddot{u}\Delta t + \ddot{a}_u \Delta t^2/2, \ddot{v}\Delta t + \ddot{a}_v \Delta t^2/2, \ddot{w}\Delta t + \ddot{a}_w \Delta t^2/2)$ in a "second-order derivable" continuous wind and acceleration field in spline formats, the initial values of the iteration may be currently taken as $u(t,x,y,z)$, $v(t,x,y,z)$, $w(t,x,y,z)$, $a_u(t,x,y,z)$, $a_v(t,x,y,z)$, $a_w(t,x,y,z)$.

Because the 3D wind and acceleration field is defined in spherical coordinates, and the 3D displacement is the motion of the upstream point to the Euler point, a straight line in Cartesian coordinates [here, we define Cartesian coordinates as $(\tilde{x}, \tilde{y}, \tilde{z})$, $\tilde{x}$ - $\tilde{y}$ plane as $\varphi = 0$ plane, $\tilde{x}$ axis as the intersection of two planes $\lambda = 0$ and $\varphi = 0$, and the origin as the center of the sphere], the upstream point and the 3D displacement must be calculated using implicit iteration based on the correspondence between Cartesian coordinates and spherical coordinates.

Let the upstream point be $(\lambda_0, \varphi_0, r_0)$, the corresponding Cartesian coordinates be $(\tilde{x}_0, \tilde{y}_0, \tilde{z}_0)$, the forecast point be (λ, φ, r), and (λ, φ, r) is also the model grid point (x, y, z). The correspondence between the right-angle coordinates and the spherical coordinates after the 3D displacement of the upstream point is:

$$\tilde{x}_0 = r\cos\varphi\cos\lambda + \Delta x\sin\lambda_0 + (\Delta y\sin\varphi_0 - \Delta z\cos\varphi_0)\cos\lambda_0 = r_0\cos\varphi_0\cos\lambda_0 \qquad (33)$$

$$\tilde{y}_0 = r\cos\varphi\sin\lambda - \Delta x\cos\lambda_0 + (\Delta y\sin\varphi_0 - \Delta z\cos\varphi_0)\sin\lambda_0 = r_0\cos\varphi_0\sin\lambda_0 \qquad (34)$$

$$\tilde{z}_0 = r\sin\varphi - \Delta y\cos\varphi_0 - \Delta z\sin\varphi_0 = r_0\sin\varphi_0 \qquad (35)$$

Equations (33)-(35) represent a system of nonlinear equations for $(\lambda_0, \varphi_0, r_0)$ and $(\Delta x, \Delta y, \Delta z)$: a "dynamic" solution based on implicit iteration is required because the former (i.e., wind speed and acceleration at the upstream point) determines the latter (i.e., 3D displacement).

Of the upstream point, the initial value of the 3D displacement, $(\Delta x_0, \Delta y_0, \Delta z_0)$, can be used to determine the initial guess values: $(\lambda_1, \varphi_1, r_1)$ and $(\tilde{x}_1, \tilde{y}_1, \tilde{z}_1)$.

Giving the "perturbation" values on the left side of equations (33)-(35): take $(\Delta x, \Delta y, \Delta z) = (\Delta x_0, \Delta y_0, \Delta z_0)$ and $(\lambda_0, \varphi_0, r_0) = (\lambda_1, \varphi, r_1)$ (left φ remains the same just at this time)to find $(\lambda_1, \varphi_1, r_1)$ and $(\tilde{x}_1, \tilde{y}_1, \tilde{z}_1)$ on the right side, we have:

$$\tilde{x}_1 = r\cos\varphi\cos\lambda + \Delta x_0\sin\lambda_1 + (\Delta y_0\sin\varphi - \Delta z_0\cos\varphi)\cos\lambda_1 = r_1\cos\varphi_1\cos\lambda_1 \qquad (36)$$

$$\tilde{y}_1 = r\cos\varphi\sin\lambda - \Delta x_0\cos\lambda_1 + (\Delta y_0\sin\varphi - \Delta z_0\cos\varphi)\sin\lambda_1 = r_1\cos\varphi_1\sin\lambda_1 \qquad (37)$$

$$\tilde{z}_1 = r\sin\varphi - \Delta y\cos\varphi - \Delta z\sin\varphi = r_1\sin\varphi_1 \qquad (38)$$

Combining equations (36)-(38), since $(36)\cdot\sin\lambda_1 = (37)\cdot\cos\lambda_1$, we can first find λ_1: $\lambda_1 = \lambda - \arcsin(\frac{\Delta x_0}{r\cos\varphi})$, and then substitute λ_1 back into equations (36)-(38) to get $(\tilde{x}_1, \tilde{y}_1, \tilde{z}_1)$, and we have: $r_1 = \sqrt{\tilde{x}_1^2 + \tilde{y}_1^2 + \tilde{z}_1^2}$, $\varphi_1 = \arcsin(\frac{\tilde{z}_1}{r_1})$.

Then, we can obtain $(\tilde{x}_2, \tilde{y}_2, \tilde{z}_2)$ as well as $(\lambda_2, \varphi_2, r_2)$ and the corresponding $(\Delta x_2, \Delta y_2, \Delta z_2)$,… from $(\lambda_1, \varphi_1, r_1)$ and the corresponding $(\Delta x_1, \Delta y_1, \Delta z_1)$. We can finally find the iterative convergent solutions $(\lambda_0, \varphi_0, r_0) = \lim_{n\to\infty}(\lambda_n, \varphi_n, r_n)$ and $(\Delta x, \Delta y, \Delta z) = \lim_{n\to\infty}(\Delta x_n, \Delta y_n, \Delta z_n)$ by repeating this cycle, but only use $n = 2$in the actual calculation.

In addition, the "forecast" wind field $(\hat{u}, \hat{v}, \hat{w})$ is obtained, $(\hat{u}, \hat{v}, \hat{w}) = (\ddot{u} + \ddot{a}_u \Delta t, \ddot{v} + \ddot{a}_v \Delta t, \ddot{w} + \ddot{a}_w \Delta t)$, and the unit vector "projection" decomposition of $(\hat{u}, \hat{v}, \hat{w})$ from the upstream point in spherical coordinates to the forecast point (called "vector discrete" decomposition) is required, and it is the same for the 3D displacement in the wind field.

We can first decompose the upstream point $(\hat{u}, \hat{v}, \hat{w})$ in spherical coordinates into rectangular coordinates, and set the decomposition as $(\tilde{u}, \tilde{v}, \tilde{w})$, and then translate and decompose $(\tilde{u}, \tilde{v}, \tilde{w})$ to the forecast point in spherical coordinates, and set the decomposition as $(u, v, w)^{t+\Delta t}$.

If for the forecast point $(0, \varphi, r)$, we have:

$$\tilde{x} : -\hat{u}\sin\lambda_0 - (\hat{v}\sin\varphi_0 - \hat{w}\cos\varphi_0)\cos\lambda_0 = \tilde{u} \tag{39}$$

$$\tilde{y} : \hat{u}\cos\lambda_0 - (\hat{v}\sin\varphi_0 - \hat{w}\cos\varphi_0)\sin\lambda_0 = \tilde{v} \tag{40}$$

$$\tilde{z} : \hat{v}\cos\varphi_0 + \hat{w}\sin\varphi_0 = \tilde{w} \tag{41}$$

Then, we have:

$$u^{t+\Delta t} = \tilde{v} \tag{42}$$

$$v^{t+\Delta t} = -\tilde{u}\sin\varphi + \tilde{w}\cos\varphi \tag{43}$$

$$w^{t+\Delta t} = \tilde{u}\cos\varphi + \tilde{w}\sin\varphi \tag{44}$$

We can find $(u, v, w)^{t+\Delta t}$ for all forecast points (λ, φ, r) using the above (equations (39)–(44)) similarly.

In addition (as with finding $(u, v, w)^{t+\Delta t}$), the 3D displacement $(\Delta x, \Delta y, \Delta z)$ of the upstream point is also decomposed to the forecast point as $(\Delta x, \Delta y, \Delta z)^{t+\Delta t}$ (the superscript $t + \Delta t$ is omitted below).

Following the completion of the wind field forecast in a single time step, the 3D displacement divergence of spherical coordinates is obtained to complete the pressure and temperature field forecast.

4.3 Pressure and temperature field forecast

4.3.1 Space-time discretization of the divergence field

The pressure and temperature field variability is determined by the 3D divergence $\nabla\cdot\mathbf{V}$ ($\nabla\cdot\mathbf{V}=(\frac{\partial u}{\partial x}+\frac{\partial v}{\partial y})_{\hat{z}}+\frac{\partial \hat{w}}{\partial \hat{z}}-\frac{v\tan\varphi}{r_e}-\frac{w_s}{\Delta Z_s}$, $w_s=u\cdot z_s^x+v\cdot z_s^y$), which determines the pressure and temperature field forecast.

First, we make a space-time discretization of $\nabla\cdot\mathbf{V}$: first we take a time-step average 3D wind speed $(\overline{u},\overline{v},\overline{w})=(\frac{\Delta x}{\Delta t},\frac{\Delta y}{\Delta t},\frac{\Delta z}{\Delta t})$, and then perform cubic spline fitting of $(\Delta x,\Delta y,\Delta z)$ in (λ,φ,z) directions respectively; then, we take a time-step average terrain lifting speed $\frac{\Delta h}{\Delta t}\triangleq\frac{\Delta x\cdot z_s^x+\Delta y\cdot z_s^y}{\Delta t}$, where Δh represent the terrain altitude difference corresponding to the horizontal upstream point to Euler forecast point (x,y,z), then we take $w_s=\frac{\Delta h}{\Delta t}$; by $z\to\hat{z}$ mathematical transformation, we can always get a time-step average 3D divergence in " spline format": $\Delta t\nabla\cdot\mathbf{V}=\Delta x^x+\Delta y^y+\Delta\hat{z}^{\hat{z}}-\frac{\Delta y\tan\varphi}{r}-\frac{\Delta h}{\Delta Z_s}$. Then, with hydrostatic horizontal divergence and non-hydrostatic vertical divergence separated: $\Delta tD_{sta}=\Delta x^x+\Delta y^y-\frac{\Delta y\tan\varphi}{r}-\overline{D}_{\hat{z}}$, $\Delta tD_{ins}=\Delta\hat{z}^{\hat{z}}-\frac{\Delta h}{\Delta Z_s}+\overline{D}_{\hat{z}}$, here $\overline{D}_{\hat{z}}=\Delta x^p p^x+\Delta y^p p^y$ is the coordinate transformation term.

4.3.2 Non-hydrostatic fully compressible pressure and temperature field forecast

The 3D divergence $\nabla\cdot\mathbf{V}$ is the one-time-step average of "starting point variability + endpoint variability" in the implicit forecast equation (equation (32)) of the upstream point, and it is used to forecast the "non-hydrostatic fully compressible" pressure field and temperature field as follows:

$$p^{t+\Delta t}=\ddot{\overline{p}}\exp(-\frac{\Delta t\nabla\cdot\mathbf{V}}{1-\kappa}) \qquad (45)$$

$$T^{t+\Delta t}=\ddot{\overline{T}}\exp(-\frac{\kappa\Delta t\nabla\cdot\mathbf{V}}{1-\kappa}) \qquad (46)$$

For the density current test in this paper, the above "non-hydrostatic fully compressible" pressure-temperature field prediction equation is used. Because the 3D divergence $\nabla\cdot\mathbf{V}$ ranges from acoustic waves (acoustic waves are compressional waves with a wave speed of about 330 m/s) to gravity waves (wave speed of about 30 m/s), only very high spatial and temporal resolutions and very short time steps (Δt of the order of 0.1 s) can be employed.

4.3.3 Hydrostatic pressure and temperature fields forecast

Based on the hydrostatic continuity equation $\frac{\partial \omega}{\partial p} = -D_{sta}$ (equation (23)) of $\hat{z}$-coordinate, cubic spline fit is performed on D_{sta}, with vertical integration of the barometric pressure difference from the top of the model down ($p_T \to p(\hat{z})$), and top layer pressure is made a constant layer ($p_T \equiv c$ and its barometric pressure variability $\omega_T \equiv 0$), then the barometric pressure variability ω or pressure increment $\omega\Delta t$ of each layer is obtained:

$$\omega\Delta t = -\int_{p_{\mathrm{T}}}^{p} D_{sta}\Delta t \mathrm{d}p \mathrel{\hat{=}} \Delta p \tag{47}$$

The pressure increment of each layer caused by the hydrostatic horizontal advection "divergence field" is represented by the above equation Δp. So, the hydrostatic pressure field forecast in each layer is then given as follows:

$$p^{t+\Delta t} = \ddot{p} + \Delta p \tag{48}$$

Then, the forecast surface pressure field is included in the above equation: $p_s^{t+\Delta t} = \ddot{p}_s + \Delta p_s$.

The adiabatic warming of the air parcel $\Delta T = \frac{\kappa \ddot{T}}{\ddot{p}} \Delta p$ is obtained from the hydrostatic horizontal advection pressurization, and the hydrostatic temperature field of each layer is forecasted:

$$T^{t+\Delta t} = \ddot{T} + \Delta T \tag{49}$$

The air pressure and temperature prediction equations presented above can describe a wide range of waves, from atmospheric long waves to gravity waves.

4.3.4 Surface pressure field forecast and atmospheric mass conservation

Though the previous equation (48) can be used to forecast the surface pressure field, the following surface pressure forecast equation can be even derived, to maintain atmospheric mass conservation.

Since the variability of surface pressure is:

$$\omega_s \mathrel{\hat{=}} \frac{dp_s}{dt} = \frac{\partial p_s}{\partial t} + u_s \frac{\partial p_s}{\partial x} + v_s \frac{\partial p_s}{\partial y} \tag{50}$$

After performing vertical integration for the hydrostatic continuity equation (equation (21)), we obtain (here let the atmosphere's top layer $p_T \to 0$):

$$\omega_s = -\int_{p_T}^{p_s} [(\frac{\partial u}{\partial x} + \frac{\partial v}{\partial y})_p - \frac{v \tan \varphi}{r}] \mathrm{d}p \tag{51}$$

The preceding equation is the integral form of the continuity equation, plugging it into equation (50) yields:

$$\frac{\partial p_{\mathrm{s}}}{\partial t} = -\int_{p_T}^{p_{\mathrm{s}}} \left(\frac{\partial u}{\partial x} + \frac{\partial v}{\partial y} - \frac{v \tan\varphi}{r}\right) \mathrm{d}p - u_{\mathrm{s}} \frac{\partial p_{\mathrm{s}}}{\partial x} - v_{\mathrm{s}} \frac{\partial p_{\mathrm{s}}}{\partial y} \tag{52}$$

By swapping the integration and differentiation orders of the first term on the right side of the above equation, we get:

$$\frac{\partial p_{\mathrm{s}}}{\partial t} = \frac{-1}{r\cos\varphi}\left(\frac{\partial}{\partial\lambda}\int_{p_T}^{p_{\mathrm{s}}} u\mathrm{d}p + \frac{\partial}{\partial\varphi}\int_{p_T}^{p_{\mathrm{s}}} v\cos\varphi \mathrm{d}p\right) \tag{53}$$

The global area A ($\mathrm{d}A = r^2 \cos\varphi \mathrm{d}\lambda \mathrm{d}\varphi$) integrates to zero on the right side of the above equation i.e.,: $\int_A \frac{\partial p_s}{\partial t}\mathrm{d}A = \frac{\partial}{\partial t}\int_A p_s \mathrm{d}A = 0$, and the physical meaning of this equation is the conservation of the global atmospheric mass.

In the following section, we derive the surface pressure forecast equation in the spline format while maintaining "atmospheric mass conservation."

After applying pressure difference cubic spline fitting and vertical integration to the model atmosphere of the equation (21) (here set the top of the model $p_T \equiv c$, $\omega_T \equiv 0$), the equation (53) of the same form is obtained.

Performing space-time discretization of the left side of equation (53): one-time-step average surface pressure increment $\frac{\partial p_s}{\partial t} = \frac{p_s^{t+\Delta t} - p_s^t}{\Delta t}$ is taken, i.e., each time step $\int_A (p_s^{t+\Delta t} - p_s^t)\mathrm{d}A = 0$ must be proved.

Performing space-time discretization of the right side of equation (53): take a time step average horizontal wind speed $(u, v) = \frac{(\Delta x, \Delta y)}{\Delta t}$ and plug it into equation (53), and then perform pressure difference cubic spline fitting and vertical integration on the "model atmosphere" of $(\Delta x, \Delta y)$, and define:

$$([u],[v]) \triangleq \frac{1}{\Delta t}\left(\int_{p_T}^{p_s} \Delta x \mathrm{d}p, \int_{p_T}^{p_s} \Delta y \mathrm{d}p\right) \tag{54}$$

The equation above $([u],[v])$ represents the horizontal wind speed of one-time-step average and air pressure (air mass) weight. When $\partial x = r\cos\varphi\partial\lambda$ and $\partial y = r\partial\varphi$, are considered, equation (53) becomes:

$$\frac{p_s^{t+\Delta t} - p_s^t}{\Delta t} = \frac{-1}{r\cos\varphi}\left(\frac{\partial[u]}{\partial\lambda} + \frac{\partial([v]\cos\varphi)}{\partial\varphi}\right) = -\left(\frac{\partial[u]}{\partial x} + \frac{\partial[v]}{\partial y}\right) + \frac{[v]\tan\varphi}{r} \tag{55}$$

For the above equations $[u]$ and $[v]\cos\varphi$, performing latitude circle and longitude circle periodic cubic spline, respectively, the following equations are converted to the spline format:

$$\frac{p_s^{t+\Delta t} - p_s^t}{\Delta t} = -\frac{[u]^\lambda + ([v]\cos\varphi)^\varphi}{r\cos\varphi} = -([u]^x + [v]^y) + \frac{[v]\tan\varphi}{r} \tag{56}$$

On the right side of the above equation, the global area integrates to zero, and we have:

$$\int_A \frac{p_s^{t+\Delta t} - p_s^t}{\Delta t}\,\mathrm{dA} = -\int_A [[u]^\lambda + ([v]\cos\varphi)^\varphi] r\,\mathrm{d}\lambda\,\mathrm{d}\varphi = 0 \tag{57}$$

The above equation makes use of the periodic cubic spline's mathematical property. Specifically, the wind field "slope" closure integrates to zero, the first term on the right side integrates to zero for the latitude circle, and the second term integrates to zero for the longitude circle. The equation (57) is then transformed into the "atmospheric mass conservation" surface pressure forecast equation:

$$p_\mathrm{s}^{t+\Delta t} = p_\mathrm{s}^t + \Delta p_s,\ \ \Delta p_s = -\Delta t([u]^x + [v]^y - \frac{[v]\tan\varphi}{r}) \tag{58}$$

Because both calculate the 3D horizontal advection, the ideal test shows that the previous equation (48) is very similar to the above equation (58) in forecasting the surface pressure field (there is a slight difference between the two, which may be attributed to the rounding error in the summation of the vertical integration of equation (54). As a result, the former is transformed to the latter using the "Poisson equation," and the surface pressure and temperature fields are redone to maintain the model's atmospheric mass conservation.

4.3.5 Time-split integration scheme

In the atmosphere, there are stable and unstable stratifications, and the unstable stratifications are further subdivided into weakly and strongly unstable stratifications.

Stable stratification (including neutral stratification): In the $t + m\delta t$ ($m = 1,2,\ldots,M$, $M\delta t = \Delta t$) time process, horizontal advection remains in the $\hat{z}$ plane (where $\hat{w} = 0$) and vertical convection remains as "half-wave oscillation": the non-hydrostatic D_{ins} term works to forecast "fully compressible" pressure and temperature fields. It includes the topographic uplift item $\frac{w_s}{\Delta Z_s}$, but, in a δt, the oscillation the item $\frac{\partial\hat{w}}{\partial\hat{z}}$ produced will recover and the air column tends to be in hydrostatic equilibrium (vertical divergence $\frac{\partial\hat{w}}{\partial\hat{z}} \to 0$ and vertical acceleration $a_w \to 0$ in air column layers).

Weakly unstable stratification (with wet unstable stratification): In the $t + m\delta t$ time course, the stratification is adjusted to stable stratification by dry convection adjustment or wet convection adjustment, or it remains weakly unstable, so the “half-wave oscillation” can also be used to describe the “full compressible” pressure, temperature fields forecast of non-hydrostatic D_{ins} term. The wet convection adjustment, on the other hand, entails “cumulus convection parameterization and precipitation,” “air mass (water vapor) source–sink and latent heat of phase change,” etc., all of which react to pressure and temperature fields.

Strongly unstable stratification: Within a time step, under the action of pressure gradient force ($a_w \neq 0$), there is always strong vertical motion, with strongly unstable stratification (such as the downburst, tornadoes, etc.) maintained, so the “half-wave oscillation” cannot be used to describe the strong vertical motion. Only 3D divergence $\nabla \cdot \mathbf{V}$ can be used to directly forecast the “fully compressible” pressure and temperature field; as a result, the mesoscale model must be nested, acoustic waves must be distinguished, very short time steps must be taken, and the wet convection adjustment process must be incorporated.

For “time-split”: if the vertical displacement is found by $\Delta z = w\Delta t + a_w \dfrac{\Delta t^2}{2}$ (and thus $\Delta\hat{z}$ and vertical divergence $\Delta\hat{z}^{\hat{z}}$), the time step should be very short because the non-hydrostatic equilibrium generates an acoustic wave that oscillates several times in one-time step (a_w changes symbol several times); as a result, the hydrostatic vertical displacement $\Delta z = z - Z$ (“half-wave oscillation” process) is carried out instead of it to block the acoustic waves.

The acoustic wave scheme calculation (“half-wave oscillation” process) is as follows:

For the convenience of description, let the pressure and temperature field at time *t* be (p^t, T^t), which becomes (p, T) after a long time step (Δt) of horizontal advection and D_{sta}, and becomes $(p^{t+m\delta t}, T^{t+m\delta t})$ after a short time step (δt) of vertical convection and D_{ins}, $m = 1,2,\ldots,M$.

① By (p, T), the initial guess value $D_{ins}\delta t = \dfrac{1}{M}(0 - \dfrac{\Delta h}{\Delta Z_s} + \overline{D}_{\hat{z}})$ (all compressible “Poisson equation” process): $(p^{t+\delta t}, T^{t+\delta t})^0 = [p\exp(-\dfrac{D_{ins}\delta t}{1-\kappa}), T\exp(\dfrac{-\kappa D_{ins}\delta t}{1-\kappa})]$ is obtained;

② (hydrostatic equilibrium equation) $\frac{\partial \ln p}{\partial z} = -\frac{g}{\mathrm{R}(T^{t+\delta t})^0}$, by "half-wave oscillation," it is obtained that: $z^1 = \int_{(p_s^{t+\delta t})^0}^{(p^{t+\delta t})^0} \frac{\mathrm{R}(T^{t+\delta t})^0}{g} d\ln p$, $\Delta z^1 = z^1 - Z$, $(\ln p^{t+\delta t})^1 = (\ln p^{t+\delta t})^0 - \frac{g\Delta z^1}{\mathrm{R}(T^{t+\delta t})^0}$, $(T^{t+\delta t})^1 = (T^{t+\delta t})^0 + \frac{\partial T}{\partial \hat{z}}\Delta z^1$;

③ Replace "0" with "1",…, "n-1" with "n", repeat the ② process to obtain: Δz^2 and $(p^{t+\delta t}, T^{t+\delta t})^2$, …, Δz^n and $(p^{t+\delta t}, T^{t+\delta t})^n$, which should theoretically take $(p^{t+\delta t}, T^{t+\delta t}) = \lim_{n\to\infty}(p^{t+\delta t}, T^{t+\delta t})^n$ and $\Delta z^n \to 0$;

The above ②-③ is the "implicit iteration" process for calculating the non-hydrostatic "half-wave oscillation" on the air column: based on the $(p^{t+\delta t}, T^{t+\delta t})^0$ after the "full compressible" process, $(p^{t+\delta t}, T^{t+\delta t})^1$ in-process is calculated, …, $(p^{t+\delta t}, T^{t+\delta t})^n$. According to the calculations, this "implicit iteration" converges in the stable stratification, i.e., to the hydrostatic equilibrium: $\frac{\partial \ln p}{\partial z} = -\frac{g}{\mathrm{R}(T^{t+\delta t})^n}$ and $\Delta z^n \to 0$. Here ($\Delta \hat{z} = \frac{z_T}{\Delta Z_s}\Delta z$), if we set $\hat{w}^n = \frac{\Delta \hat{z}^n}{\delta t}$, then $\hat{w}^n$ is the vertical velocity in the "half-wave oscillation," under the action of the pressure gradient force (a_w), $\hat{w}^n$ turns from "full compressible" to zero in "hydrostatic equilibrium" ($\hat{w}^n \to 0$, $\frac{\partial \hat{w}}{\partial \hat{z}} \to 0$ disappears in "half-wave oscillation"). In the actual "implicit iteration," only $n = 2$ is taken.

④ Replace (p, T) with $(p^{t+\delta t}, T^{t+\delta t})$, repeat the ①-③ process for M times to obtain $(p^{t+2\delta t}, T^{t+2\delta t})$, …, $(p^{t+\Delta t}, T^{t+\Delta t})$, thus completing the time-split integral in a time step (Δt).

Obviously, the hydrostatic dynamic frame ($D_{\mathrm{ins}} \equiv 0$) does not require ① process.

This acoustic wave calculation scheme maintains the physical mechanism of the "non-hydrostatic fully compressible" vertical motion from compressional wave "acoustic wave" to gravity wave, while effectively avoiding acoustic wave propagation.

In this study, the gravity wave test is performed using the "hydrostatic and non-hydrostatic time-split and computational acoustic wave" integration scheme above. We show that in stable stratification conditions, the order of 10s can be taken for $\Delta t = \delta t$, as if "time-split" is only a sufficient condition, not a necessary condition.

5 Model boundary with spline format

Cubic spline mathematical boundary: (i) known boundary slope of the first-order derivative or boundary curvature of the second-order derivative; (ii) periodic cubic spline. The periodic cubic spline (no boundary) should be used in the horizontal direction for the global model, and the global model provides the boundary for the nested model. The forward/backward difference boundary can be used by the temperature, humidity, and wind / displacement fields at the top and bottom of the model, and the "hydrostatic equilibrium" boundary of the pressure field at the top and bottom layer can make the vertical acceleration at the top and bottom zero. The "fully compressible" boundary of wind/displacement bottom differential changes the surface pressure field, whereas the "non-compressible" boundary does not.

The physical boundary of the rigid top layer of the model: set the air pressure at the top layer of the model $p_T \equiv c$ as a constant layer, altitude $z_T \equiv c$ as a constant layer, temperature T_T as a constant temperature layer, $q_T \equiv 0$ as a water vapor-free layer, $u_T = v_T = w_T \equiv 0$ as a stationary layer, the top layer of the model has no mass exchange, no water vapor exchange, but with net energy in and out (the ideal tests in this paper use all the rigid top layer).

6. Advection tests

6.1 Longitude-latitude grid and quasi-uniform longitude-latitude grid

In this study, a rectangle with spherical topology, a 1 °×1 °longitude-latitude grid, called an "A-grid", is described. Grids with a higher resolution can then be extrapolated to scale.

The 1 °×1 °A-grid (Table 1) has (0:360, -90:90) 65160 grid points. At the poles, 360 identical values are always allocated to the scalar field's *p*, *T*, *q*, and the vertical vector fields *w*, and 360 "trigonometric" decomposition values are always assigned to the horizontal vector fields (u, v) and (a_u, a_v) reduced.

Based on the A-grid, a quasi-uniform longitude-latitude grid, called "B-grid" (Table 1), is introduced, and the B-grid multiply reduces the forecast points in segments from the equator to the poles, and it is equidistant in latitude and coincides with the A-grid, that is $\mathrm{B} \subset \mathrm{A}$, and the forecasts are solely made for the B-grid by performing a cubic spline fitting to every latitude, to interpolate and assign forecast values to the A-grid.

N°/S°	A-grid (n/d)	B-grid (n/d)
0-59	360/1-0.52	360/1-0.52
60-74	360/0.50-0.28	180/1-0.55
75-78	360/0.26-0.21	120/0.78-0.62
79-80	360/0.19-0.17	90/0.76-0.69
81-82	360/0.16-0.14	72/0.78-0.70
83	360/0.12	60/0.73
84	360/0.10	45/0.84
85	360/0.09	40/0.78
86	360/0.07	36/0.70
87	360/0.05	30/0.79
88	360/0.03	18/0.70
89	360/0.02	12/0.52
90	360/0.00	1/0.00

Table 1. The global $1^{\circ}\bullet 1^{\circ}$ longitude-latitude grid (A-grid), the quasi-uniform longitude-latitude grid (B-grid): demote n as numbers of forecasting point in each degree of latitude, and d as latitudinal distance, e.g.:d=1, that is 1 degree distance at the equator or at a longitude.

6.2 Equilibrium flow test

To test the accuracy of the spline format and address the issue of an excessively dense grid in the polar region of the A-grid, the equilibrium flow test is carried out on the A-B grid by bicubic surface fitting and interpolation to find the horizontal motion path and forecast physical values of the upstream point.

The equilibrium flow test initial value field is designed as $q = v = w = 0$, which satisfies the hydrostatic equilibrium and horizontal motion quasi-geostrophic equilibrium, and moves around the earth's axis with a constant angular velocity, then we have (set $u_0 = 20$ ms^{-1}):

$$u(\lambda,\varphi,z) = u_0\cos\varphi \qquad (59)$$

The model atmosphere is set to a constant temperature lapse rate (let $\gamma = 0.005$ Km^{-1}):

$$\frac{\partial T}{\partial z} = -\gamma \qquad (60)$$

The pressure and temperature fields are solved as (let $\mathrm{G} = \frac{\gamma u_0}{g}(2\Omega r_e + u_0)$):

$$T(\lambda,\varphi,z) = T_0 - \gamma z - \frac{\mathrm{G}}{2}\sin^2\varphi \qquad (61)$$

$$p(\lambda, \varphi, z) = p_0 (\frac{T}{T_0})^{\frac{g}{R\gamma}} \tag{62}$$

Above, let $p_0 = 1020$ hPa and $T_0 = 300.15$ K, p_0 and T_0 be the air pressure and temperature of the ground on the equator, respectively.

After substituting the above *p, T, q, u, v, w* initial value fields into the atmospheric motion equation, it is not difficult to find a frictionless, water vapor-free process: $\frac{dp}{dt} = \frac{dT}{dt} = \frac{du}{dt} = \frac{dv}{dt} = \frac{dw}{dt} \equiv 0$, so the equilibrium flow test is the "eternal" motion of the model atmosphere in horizontal constant angular velocity. In the initial value field, *p, T, and u* fields are east-west parallel "straight lines" in any height layer (Figure 1a for the *p* field), because the path on the "straight line" flow field overlaps with the trajectory, the time integral *p, T, u* fields should remain unchanged.

(a)

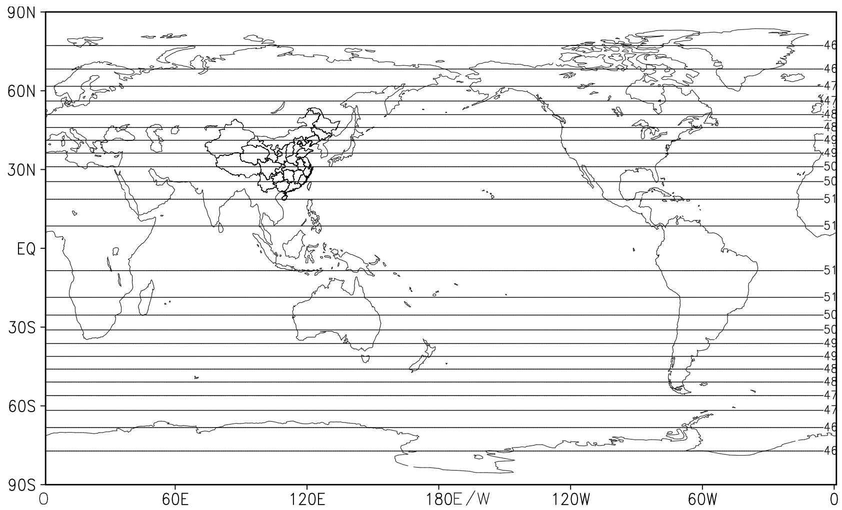

(b)

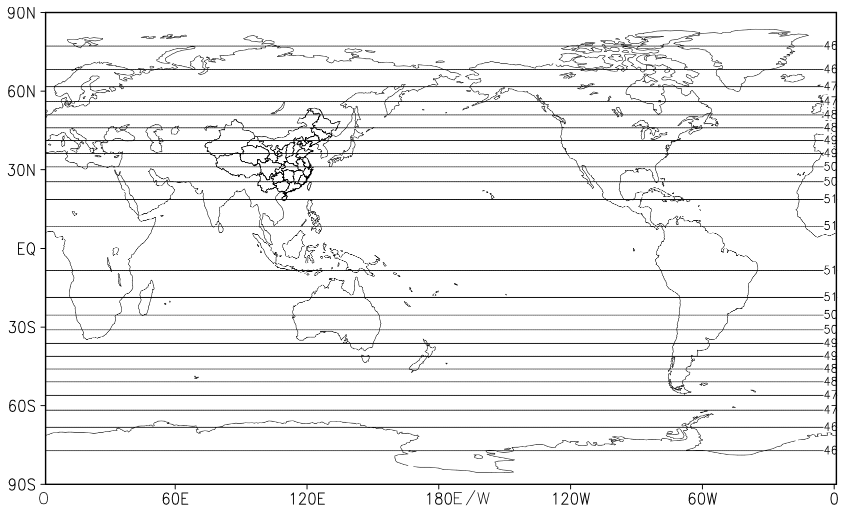

Fig.1. Equilibrium flow tests.

(a) initial pressure field (*p*: hPa, at 5749 gpm layer); (b) The same as (a), but for 30-day forecast field.

Quasi-geostrophic equilibrium flow test results: on the A-B grid mapping a global $1^\circ\times 1^\circ$ mesh, from the pressure, temperature, and wind initial value fields to the 30d integration fields, with time steps of 600s, they hardly change (Figure 1b for the *p* field) on any contour plane. The fact that atmospheric mass, energy, and momentum fields flow in parallel and uniformly, and the “cubic” advection is compatible with linear advection, shows that the nonlinear bicubic surface fitting of the linear pressure/mass), temperature/ energy, and wind/momentum fields can ensure that the horizontal path of the upstream point coincides with its trajectory.

6.3 Cross-polar flow test

We design an ideal horizontal, two-dimensional cross-polar flow test to examine the viability and accuracy of the upstream point in the spline format on the A-B grid, including the polar regions and the poles, the correctness of the procedure of the horizontal motion equation at the North Pole and the South Pole, and to address the issues of the overly dense grid in the polar region and the singularity of the poles.

Suppose the advection satisfies the geostrophic equilibrium and the initial perturbation pressure field is taken as:

$$p = p_0 \exp\left(-\frac{2\Omega r_e v_0}{\mathrm{R}T_0}\sin^3\varphi\cos\varphi\sin\lambda\right) \tag{63}$$

Suppose in the above equation, $p_0 = 1000$ hPa, $T_0 = 300$ K, $v_0 = 20$ ms^{-1}.

Then the spline format horizontal geostrophic wind $(u_\mathrm{g}, v_\mathrm{g})$ is:

$$(u_\mathrm{g}, v_\mathrm{g}) = \frac{\mathrm{R}T_0}{f}[-(\ln p)^y, (\ln p)^x] \qquad \left(-\frac{\pi}{2} \le \varphi < 0, 0 < \varphi \le \frac{\pi}{2}\right)$$

$$u_\mathrm{g} = v_\mathrm{g} = 0 \qquad (\varphi = 0) \tag{64}$$

and the initial value of the horizontal geostrophic wind is obtained as:

$$u_\mathrm{g} = v_0(3\cos^2\varphi - \sin^2\varphi)\sin\varphi\sin\lambda \ , \quad v_\mathrm{g} = -v_0\sin^2\varphi\cos\lambda \tag{65}$$

The cross-polar flow is characterized by (Figure 2): $(u_\mathrm{g})_N = 0$, $(v_\mathrm{g})_N = -v_0$ at the North Pole; $(u_\mathrm{g})_S = 0$, $(v_\mathrm{g})_S = -v_0$ at the South Pole, which is consistent with the definition of horizontal wind at the pole; and $u_\mathrm{g} = v_\mathrm{g} \equiv 0$ the equator.

From equation (6), it is found that the exact solution of the geostrophic wind keeps parallel / perpendicular to the perturbed pressure field contour / gradient, and the path of the upstream point obtained by the flow line should coincide with the trajectory, without change of the mass field.

Log-pressure ($\ln p$) field of each layer is fitted to a spherical bicubic surface, allowing for a diagnosis of the horizontal geostrophic wind (Figure 2a).

The cross-polar flow test with a horizontal resolution of $1^\circ \times 1^\circ$ is designed (Table 2):

Cross-polar flow tests	Geostrophic wind	Time step	Integration time
Test 1	(u_g, v_g)	300 s	10 d
Test 2	$(u_g + 5\cos\varphi, v_g)$	300 s	10 d

Table 2. Cross-polar flow tests.

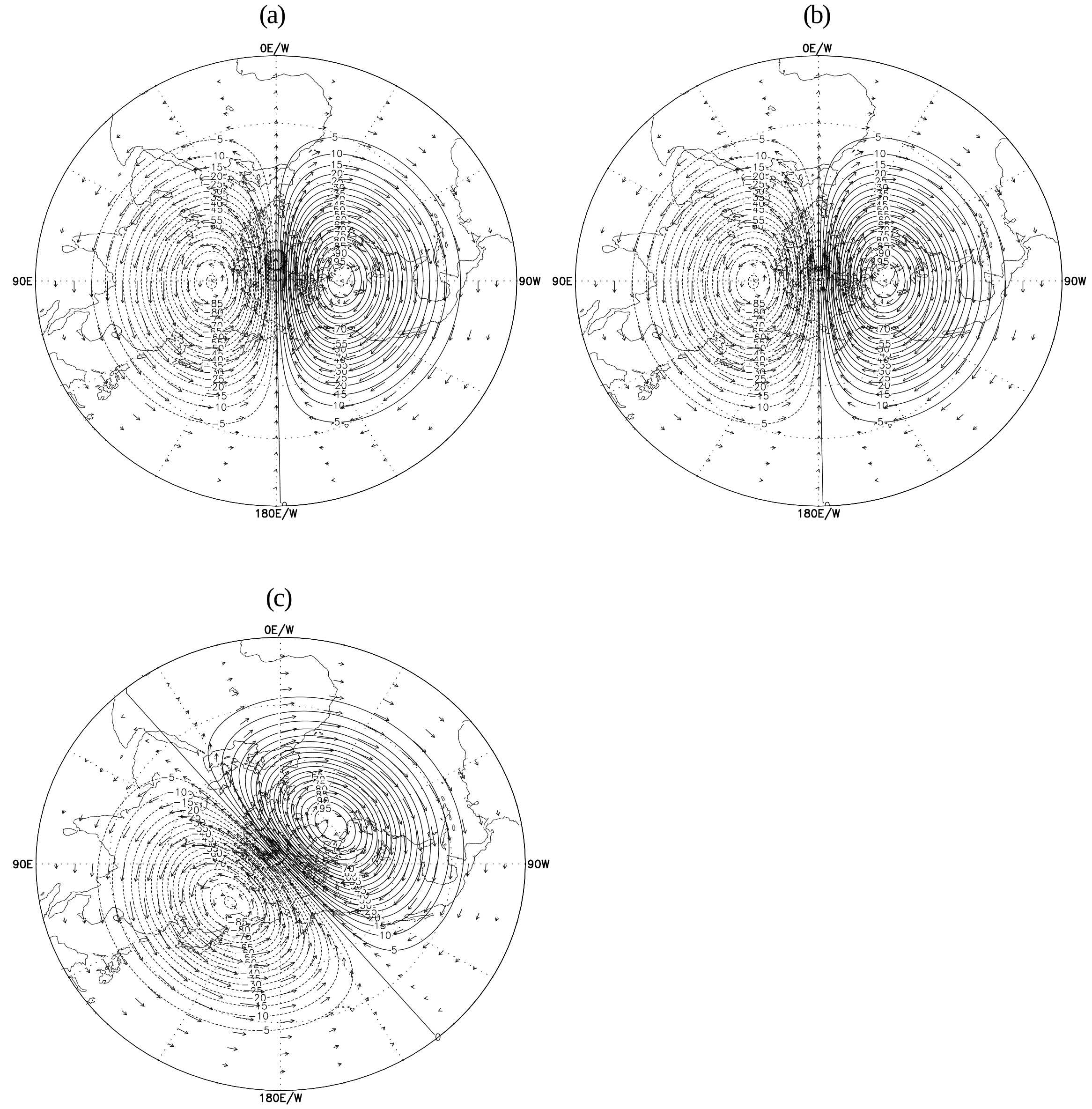

Fig. 2. Cross-polar flow test.

(a) initial ground perturbation pressure field (p: hPa) and geostrophic wind field (m/s); (b) Test 1, 10 d forecast field with (u_g, v_g); (c) Test 2, 10 d forecast field with $(u_g + 5\cos\varphi, v_g)$.

The perturbation pressure/mass field should not change over time, and the geostrophic wind in Test 1 should maintain its parallel alignment with the isobars; however, in Test 2, with a constant angular velocity applied ($5\cos\varphi\,\mathrm{ms}^{-1}$), plus the effect of the advection, the perturbation pressure/mass field can only rotate uniformly.

The results of the cross-polar flow test (see Figure 2 for the Northern Hemisphere): compared with the initial value field (Figure 2a), the wind and pressure fields in Test 1 hardly change with time (Figure 2b); in Test 2, after being integrated for 10d (Figure 2c), the geostrophic wind and pressure field relationship is maintained globally, including polar regions, and the perturbation pressure/mass field has little deformation, little mass change despite wind and pressure field rotation.

6.4 Rossby–Haurwitzwave test

The Rossby–Haurwitz wave, often known as the “R-H wave,” is an approximate solution to the linear barotropic vorticity equation that, given certain assumptions becomes an exact solution.

If the Coriolis force ($f = 2\Omega \sin\varphi$) changes slowly and only describes the R-H wave in the Northern Hemisphere, so f is set at 45°N and taken as $f = f_0 = 2\Omega \sin(\frac{\pi}{4})$ then let the perturbed geopotential height field h of the R-H wave (the exact solution):

$$h(\lambda,\varphi,z) = 2\Omega \sin(\frac{\pi}{4})\frac{\psi(\lambda,\varphi,z)}{g} \tag{66}$$

Where, ψ is a stream function, having a wind-pressure field relationship with the divergence-free wind (u_ψ, v_ψ):

$$(u_\psi, v_\psi) = (-\frac{\psi^\varphi}{r_e}, \frac{\psi^\lambda}{r_e \cos\varphi}) \tag{67}$$

According to the aforementioned equation (9), the path of the upstream point generated by the flow line will coincide with the trajectory, without changing the mass field. Similarly, the divergence-free wind stays exactly parallel / perpendicular to the stream function field contour / gradient.

Suppose h_0 ($h_0 = 300$ gpm) be the disturbance amplitude, and take $u_0 = 20$ m/s, and let $\mathrm{C} = \frac{gh_0}{r_e f_0}$, and set the “4-latitudinal wave” stream function field ψ as:

$$\psi = \mathrm{C}\cos^2\varphi\cos(4\lambda) + r_e u_0(1-\sin\varphi) \hat{=} \psi 1 + \psi 2 \tag{68}$$

Substituting equation (68) into equation (67), we get:

$$u_\psi = u_{\psi 1} + u_{\psi 2} \;:\; u_{\psi 1} = \mathrm{C}\sin(2\varphi)\cos(4\lambda) \;,\; u_{\psi 2} = u_0 \cos\varphi$$

$$v_\psi = -4\mathrm{C}\cos\varphi\sin(4\lambda) \tag{69}$$

Where, $u_{\psi 2}$ is the latitudinal constant angular velocity.

ψ is fitted to a spherical bicubic surface before each time step integration to obtain its slope ψ^x and ψ^y, then we have a wind-pressure field relationship in “spline format” (compare with equation (67)):

$$(u_\psi, v_\psi) = (-\psi^y, \psi^x) \tag{70}$$

Here, only two-dimensional, ground-level R-H wave advection tests are performed.

First, the height amplitude h_0 is converted to "isothermal atmospheric" pressure amplitude p_0, that is, the geopotential height perturbation field is converted to pressure perturbation field, then we have (let $p_N = 840$ hPa, $T_N = 273.15$ K, p_N, T_N be the ground North Pole pressure and temperature, T_N also be the isothermal atmospheric temperature):

$$p_0 = p_N[1 - \exp(-\frac{gh_0}{\mathrm{R}T_N})] \quad (71)$$

Here, three R-H wave tests are designed (Table 3):

Rossby-Haurwitz wave	Divergence-free wind field	Time step	Time integral
Test 1	$(u_{\psi 1} + 20\cos\varphi, v_{\psi})$ m/s	600 s	100 d
Test 2	$(u_{\psi 1} + 30\cos\varphi, v_{\psi})$ m/s	600 s	100 d
Test 3	$(u_{\psi 1} + 30\cos\varphi, v_{\psi})$ m/s	600 s	300 d
Test 4	$(u_{\psi 1} + 30\cos\varphi, v_{\psi})$ m/s	60 s	300 d

Table 3. Rossby–Haurwitz wave tests.

(a) (b)

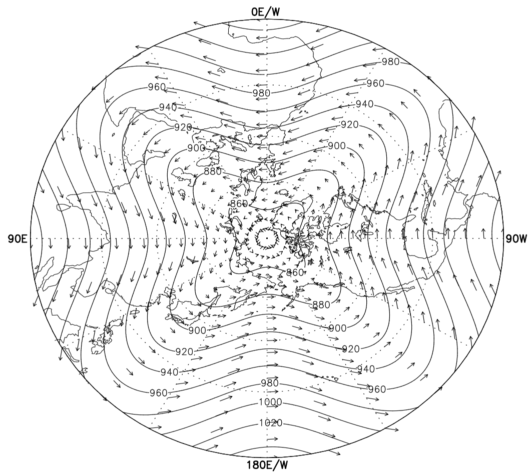

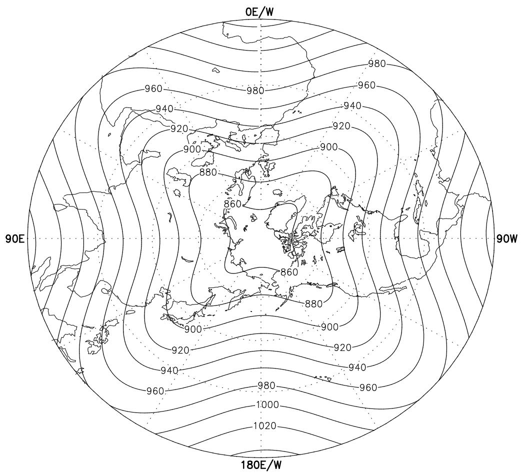

(c) (d)

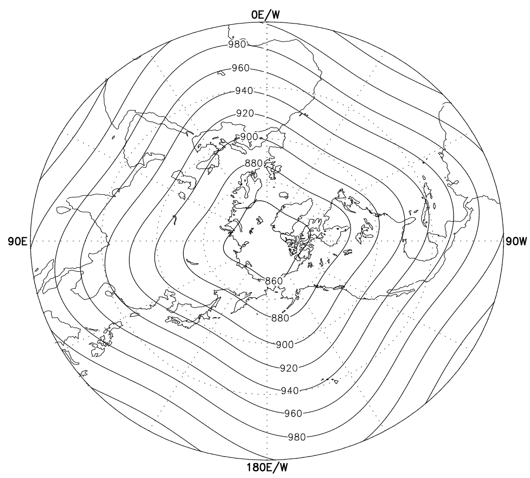

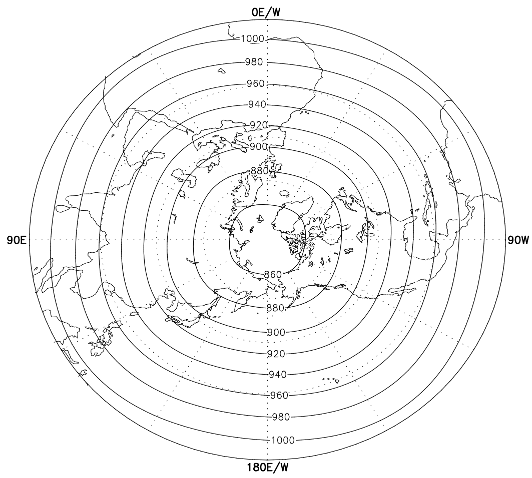

(e)

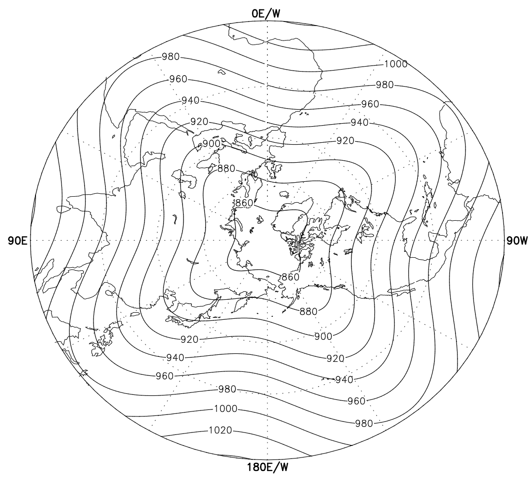

Fig. 3. Rossby–Haurwitz wave test.

(a) Initial sea level pressure field and horizontal divergence-free wind field; (b) Test 1, 100d forecast field with $(u_{\psi 1}+20\cos\varphi, v_{\psi})$ m/s and $\Delta t = 600s$; (c) Test 2, 100d forecast field with $(u_{\psi 1}+30\cos\varphi, v_{\psi})$ m/s and $\Delta t = 600s$; (d) Test 3, The same as Test 2, but for 300d forecast field; (e) Test 4, The same as Test 3, but for $\Delta t = 60s$

Results of the R-H wave test (see Figure 3 for the Northern Hemisphere and Figure 3a for the initial value field):

Test 1 flow field has a constant equal latitudinal angular velocity $u_{\psi 2} = 20\cos\varphi$ (m/s). The path of the upstream point remains parallel to the trajectory, the forecast flow function or mass field does not rotate, and bicubic surface fitting can preserve the spherical symmetry of the original flow field, and 100d integrated perturbed pressure/mass field has insignificant deformation and error. Additionally, the divergence-free wind-pressure field relationship is maintained (Figure 3b).

Tests 2-4 all added another $10\cos\varphi$ (m/s) of equal latitudinal angular velocity: they turn as $u_{\psi 2} = 30\cos\varphi$ (m/s) (Table 3). In Test 2, under the action of the advection $(u_{\psi 1} + 30\cos\varphi, v_{\psi})$ m/s, the pressure / mass field rotates due to the addition of the zonal angular velocity, and the deformation of the 100d integrated “rotating” mass field (Figure 3c) is a lot larger than that in Test 1 (Figure 3b), and when the integration is extended to 300d in Test 3, the pressure field has closely become “round” (Figure 3d). The 300d predicted air pressure field in Test 4 (Figure 3e) has much more “fidelity” than that in Test 3 (Figure 3d), but with a time step of the 60s, that is 10 times higher time precision while the computation volume also grows by 10 times.

The R-H wave test proved that using spline forecast, the amplitude error of wave, that can be pressure field becomes “round”, is monotonically bounded, and correct fluctuation phase propagation, which means that phase propagation is independent of spatial resolution, is maintained, and there is convergence between fidelity and time resolution.

7 Density flow test

7.1 Initial value field

The divergence field comprises acoustic wave propagation, and the density flow test calculates the non-hydrostatic fully compressible air parcel displacement, divergence, and pressure and temperature field fluctuation.

The density flow test is a two-dimensional (x, z) ideal field test, the initial value field is still taken as a 3D model atmosphere, but only the middle vertical cross-section grid points in the y-direction is used for the time integration, and each time step is given the same forecast values for the other grid points in the y-direction, then it is set $P^{y} = P^{xy} \equiv 0$. The typical density flow test has a spatial resolution of $\Delta x = \Delta z = 100$ m without topography, (x, y, z) the area is taken as $(0{:}512, -4{:}4, 0{:}53)$, then it always is set $P(x, y, z) \equiv P(x, 0, z)$.

The *x*-direction is a periodic cubic spline, which means that there are no boundaries; the y-direction is the rigid boundary $P^y \equiv 0$; the z-direction top and bottom layer: the air pressure and the perturbation pressure are the hydrostatic equilibrium boundary, making the top and bottom layer $w = a_w \equiv 0$. While temperature, wind, and displacement are all the forward and backward difference boundaries, which make the divergence act on and change the surface pressure and temperature field on the bottom layer, to cause the surface pressure to become completely elastic, yet the top layer air pressure, temperature ,and wind all remain constant.

The undisturbed initial value field is the dry hydrostatic atmosphere, $q = u = v = w = 0$, the ground pressure is 1000 hPa, and the model atmospheric initial potential temperature (θ) field is 300 K, then the ground layer temperature is 300 K.

In the center of the undisturbed initial value field, a circular, cross-section cold surge is placed (Figure 4), that is, set:

$$\Delta\theta = \frac{-15}{2}[\cos(\pi \cdot \mathrm{L}) + 1] \quad ,$$

$$\mathrm{L} = \sqrt{\left(\frac{x_\mathrm{i} - x_\mathrm{c}}{\mathrm{r}_x}\right)^2 + \left(\frac{z_\mathrm{k} - z_\mathrm{c}}{\mathrm{r}_z}\right)^2} \le 1 \quad , \qquad \mathrm{i}=0,1,\ldots 512; \ \mathrm{k}=0,1,\ldots 53 \qquad (72)$$

here (Figure 4), take $(x_\mathrm{c}, z_\mathrm{c}) = (256\times100\ \mathrm{m},\ 30\times100\ \mathrm{m})$ as the cold surge center point, $(\mathrm{r}_x, \mathrm{r}_z) = (40\times100\ \mathrm{m},\ 20\times100\ \mathrm{m})$ is the cold surge (x, z) direction radius, in the cold surge center point: $\mathrm{L} = 0$, $\Delta\theta$ =-15 K. Using the hydrostatic force equation and the potential temperature conservation Poisson equation, the perturbation initial value field pressure and temperature distribution are obtained. Because of the cold surge, the initial value of the air pressure field changes a little; for example, the ground pressure directly below the cold surge center reaches 1013.21 hPa.

Using the separation hydrostatic pressure method, the "time-varying reference atmosphere" and vertical acceleration a_w is calculated at each time step, and then the initial value field a_w is a non-null distribution only in the cold surge.

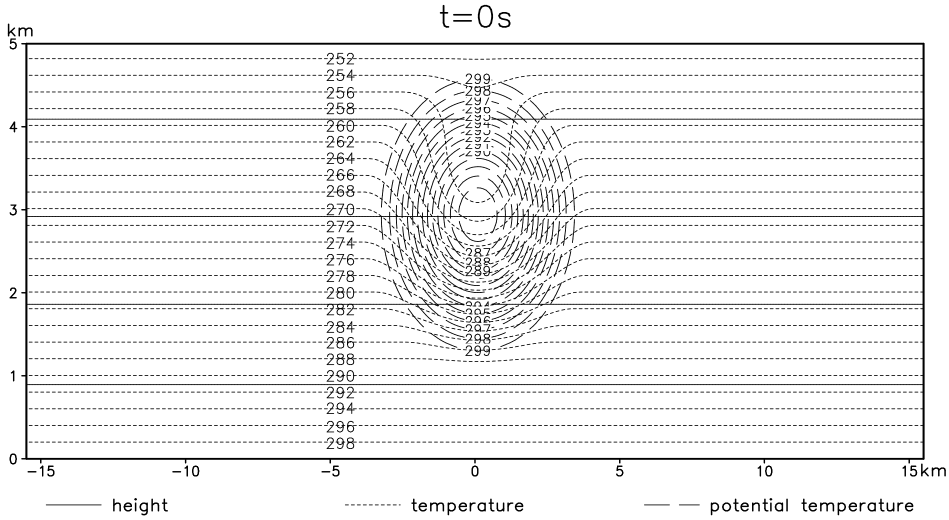

Fig. 4. Density flow test.

Initial value field: height (solid line: hPa), temperature (dotted line: K), and potential temperature (dashed line: K) for Test 1 with time step 0.1 s and Test 2 with 0.125 s.

7.2 Temporal resolution and spatial smoothing

The density flow test benchmark reference solution takes a time step of 0.1s, with a time integration of 900s.

Density flow Test 1 (Figure 5), with a time step of 0.1s; three-point spatial smoothing with a vertical wind field coefficient of 1/3, and the three-point smoothing with a horizontal pressure field coefficient of 1/2 are performed every three-time steps (0.3s). In the smoothing of the barometric field, corresponding Poisson equation “adiabatic temperature change” smoothing is performed on the temperature field (called “potential temperature conservation” pressure, temperature field smoothing).

Similar to Test 1, but with a 0.125s time step, is the density flow Test 2 (Figure 6). A vertical wind field smoothing, a pressure and temperature field “potential temperature conservation” smoothing; and three-point smoothing with divergence field horizontal and vertical coefficients of 1/2 are also carried out every time step (0.125 s), respectively, to prevent the growth and propagation of the acoustic waves.

Density flow Test 1 and Test 2 both extend the integration to 1200s, and the results of both tests are roughly similar (Figures 5 and 6).

In addition to the benchmark reference solution being in a higher-order precision spline format (its linear principal part is second-order central difference), they also have different boundary conditions and spatial smoothing schemes. Straka et al. (1993) proposed the density flow test benchmark reference solution n linear format with various resolutions.

7.3 Density flow test analysis

A highly nonlinear density flow test revealed the whole “cold surge sinking → bottom cold air accumulation → Kelvin-Helmholtz horizontal wind shear formation at cold front → unstable vortex formation” evolution process, and it is an “acoustic + gravity wave” propagation process.

Density flow test (Figures 5 and 6): under negative buoyancy of the vertical pressure gradient force, the cold surge accelerated sinking, and cold surge accumulates after hitting the bottom, forming sinking divergence “cold front” air flow. The cold air is divided into two (for a 3D test, cold air shall be in circular fluctuation) symmetric cold fronts on the left and right (Figures 5 and 6 only show a forward movement along *x*).

Results of the density flow test show that after 300 s of integration, the cold surge main body reaches the bottom, forming a strong horizontal wind vertical shear in front of the cold front, achieving Kelvin-Helmholtz shear instability. This forms the first front vortex (Figures 3① and 4①); after 600 s of integration, the first vortex rapidly intensified, with “multi-vortex” rolling on the back, while the front forms a second vortex (Figures 3② and 4②); integrated for 900 s, the first vortex has developed into a circular vortex, and the second vortex is still developing, followed by the development of a third vortex (Figures 3③ and 4③); integrated for the 1200 s, the cold front continues to move forward, with three-vortex pattern maintained roughly (Figures 3④ and 4④).

(Figures 7 and 8) Before the cold surge reaches the bottom, the ground pressure directly below the cold surge center drops rapidly, once down to about 1002 hPa. During this process, the layer of near-ground 900 m keeps in sinking motion, with vertical wind speed reaching about -14 ms^{-1} when being integrated into for 200s. The cold surge process is divided into forward compression and rebound (the so-called “fully compressible” = “fully elastic”); when the cold surge hits the bottom for the first time, the surface pressure once again increased to 1013 hPa, then first rebounds, the pressure goes back to about 1005 hPa, with a big shock wave amplitude of about 7-8 hPa, shock process about the 30 s, followed by a number of small “fully elastic” waves with an amplitude of about 3 hPa. The big shock wave is a gravity wave, with an interval of about 150 s, and it weakens toward “undisturbed surface pressure of 1000 hPa.” Similar to the surface pressure changes directly below the cold surge center, the surface pressure 10km right of the cold surge also presents shock wave evolution with wave amplitude from about 4 hPa to about 1hPa, and interval of about 75 s; that is, the latter has smaller amplitude but the higher frequency, which shows the gravity wave horizontal propagation and divergence characteristics. At the same time, the maximum vertical wind at 900 m above 10 km in front of the cold surge is 7.5 ms^{-1} when a cold front passes, then, the rising wind speed is rapidly reduced, too -1 ms^{-1} sinking motion once, and back to 5.5 ms^{-1} rising motion when the secondary cold front passes.

(Figure 9) The surface horizontal wind directly below the cold surge presents acoustic vibration, with an acoustic amplitude of about 0.002 ms^{-1}, and the surface horizontal wind 10km ahead of the cold surge shows gravity wave characteristics; corresponding to the addition of the aforementioned vertical wind, the horizontal wind speed gradually increased before the passage of the cold front, reaching a maximum speed of 23 ms^{-1} when the front passed after being integrated for 600s. It is clear that the evolution of horizontal wind includes the propagation of acoustic and gravity waves, with the gravity "fast" wave having a 1 ms^{-1} periodic oscillation amplitude superimposed.

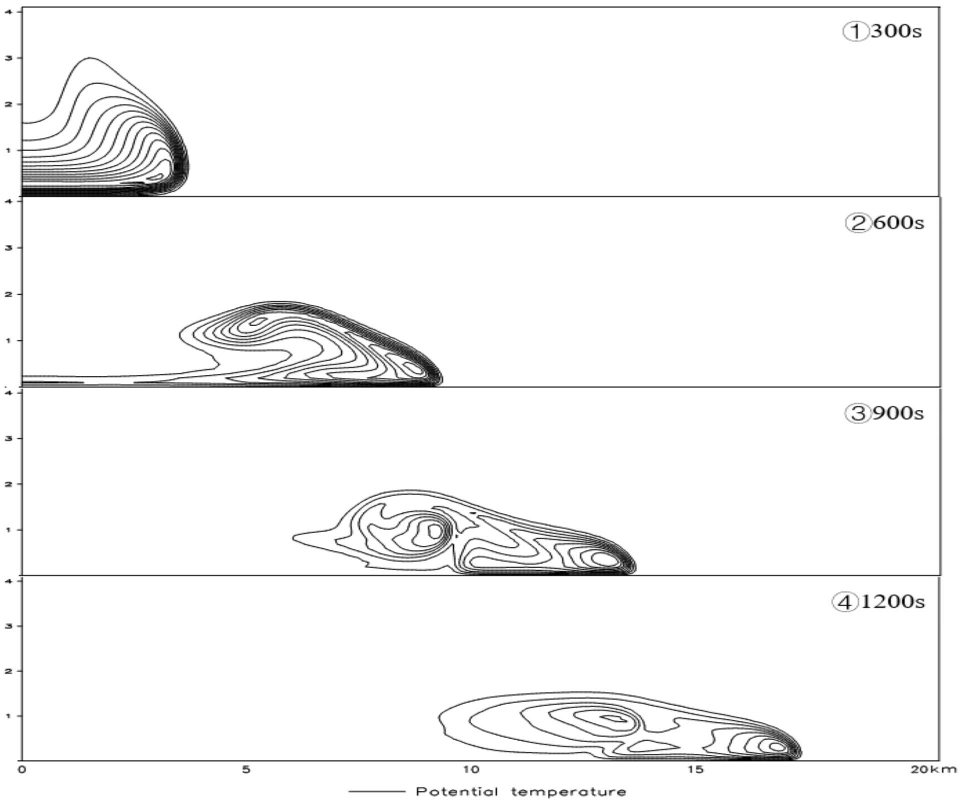

Fig. 5. Density flow Test 1. Time step 0.1 s, potential temperature (solid line: K) forecast field (only shows a forward movement of symmetrical motion along x): integrated for ①300 s; ②600 s; ③900 s; ④1200 s.

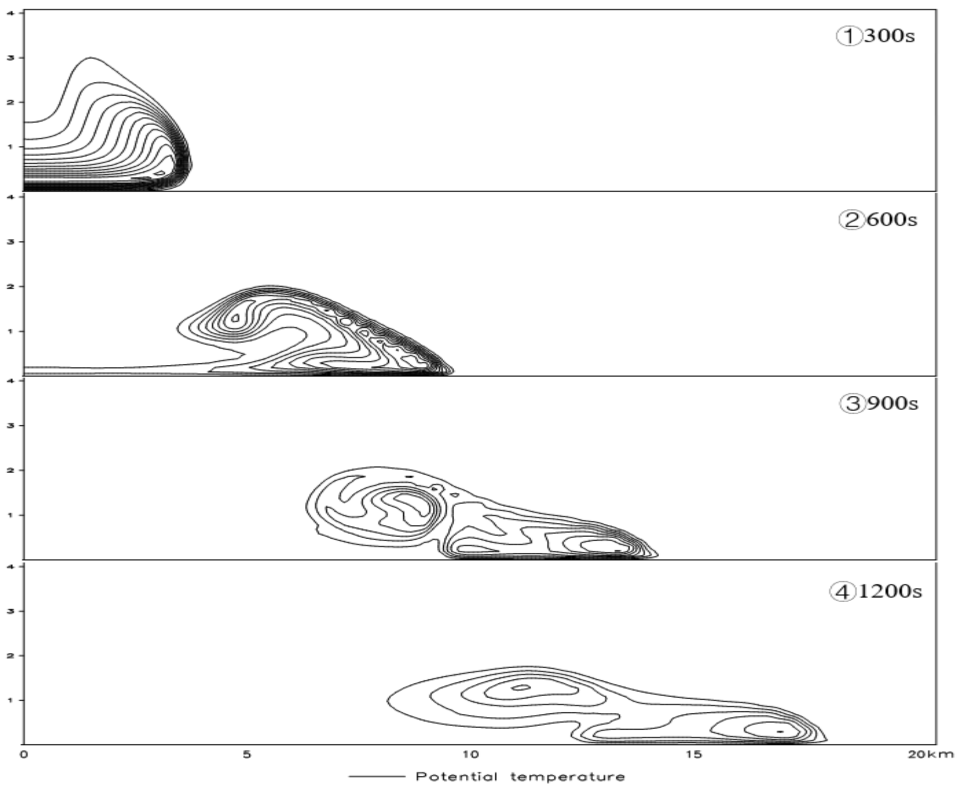

Fig. 6. Density flow Test 2. Time step 0.125 s, the forecast field is the same as that of density flow Test 1, but with different spatial smoothing schemes.

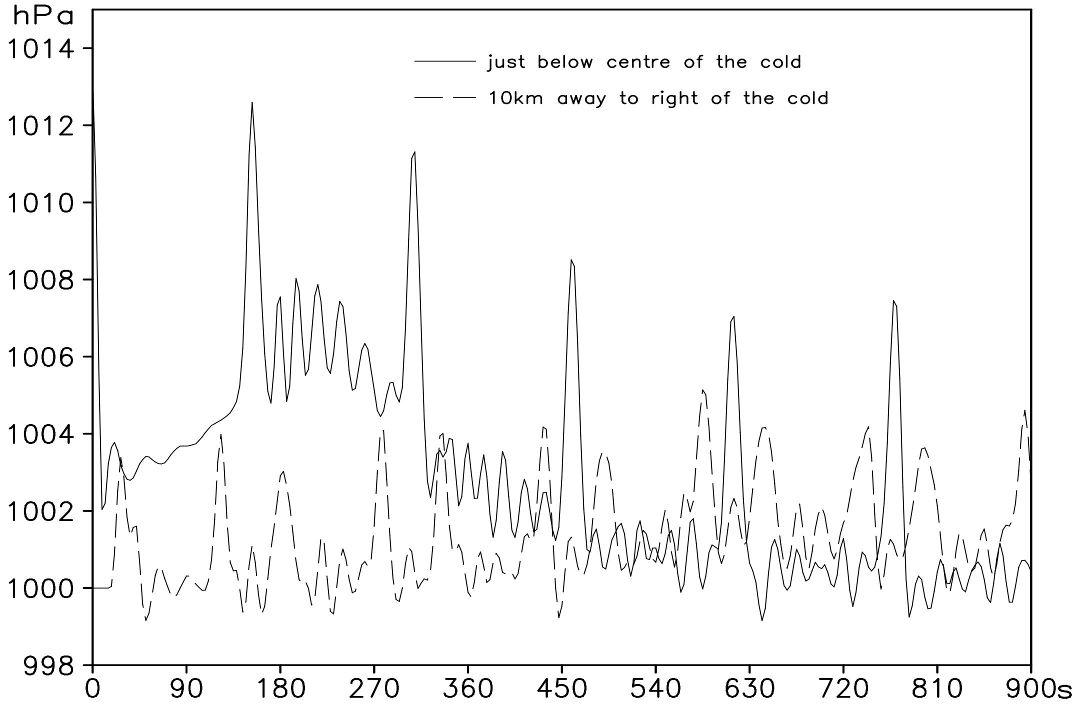

Fig. 7. Ground pressure change curve diagram of the density flow Test 1.

Simulating surface pressure at the cold surge center (solid line: hPa), simulating surface pressure 10 km to the right of the cold surge (dashed line: hPa), integrated for 900 s.

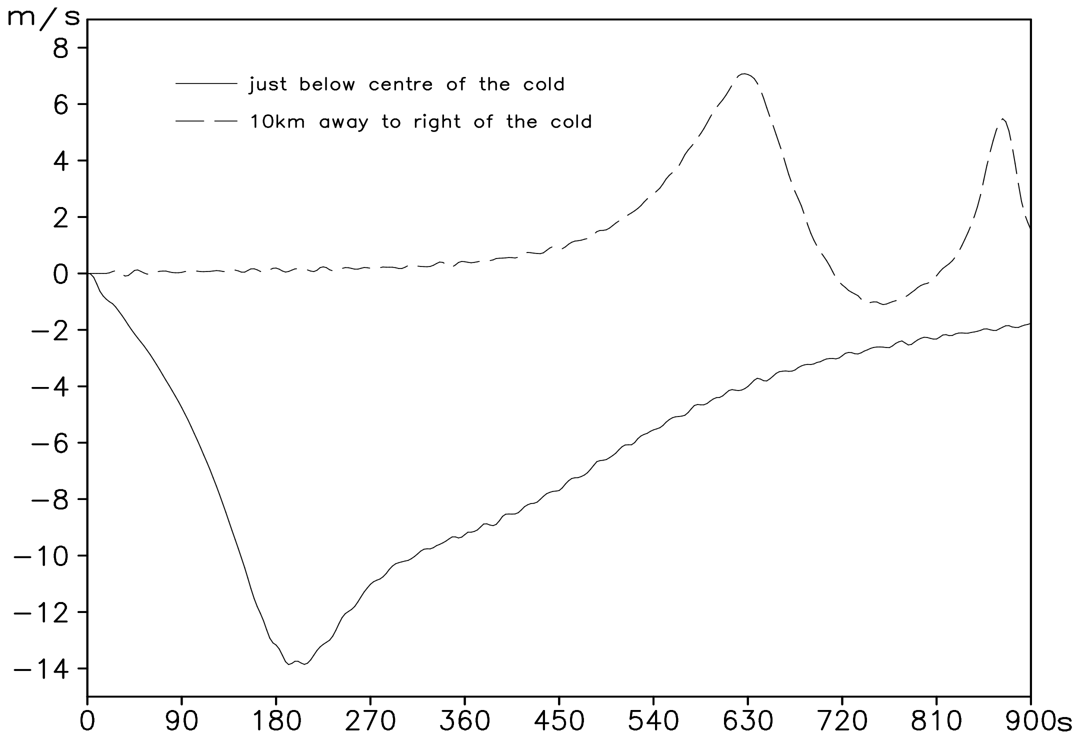

Fig.8. Vertical wind change curve diagram of the density flow Test 1.

Near-ground 900 m vertical wind at the cold surge center (solid line: $m \cdot s^{-1}$), near-ground 900 m vertical wind 10 km to the right of the cold surge (dashed line: $m \cdot s^{-1}$), integrated for 900 s.

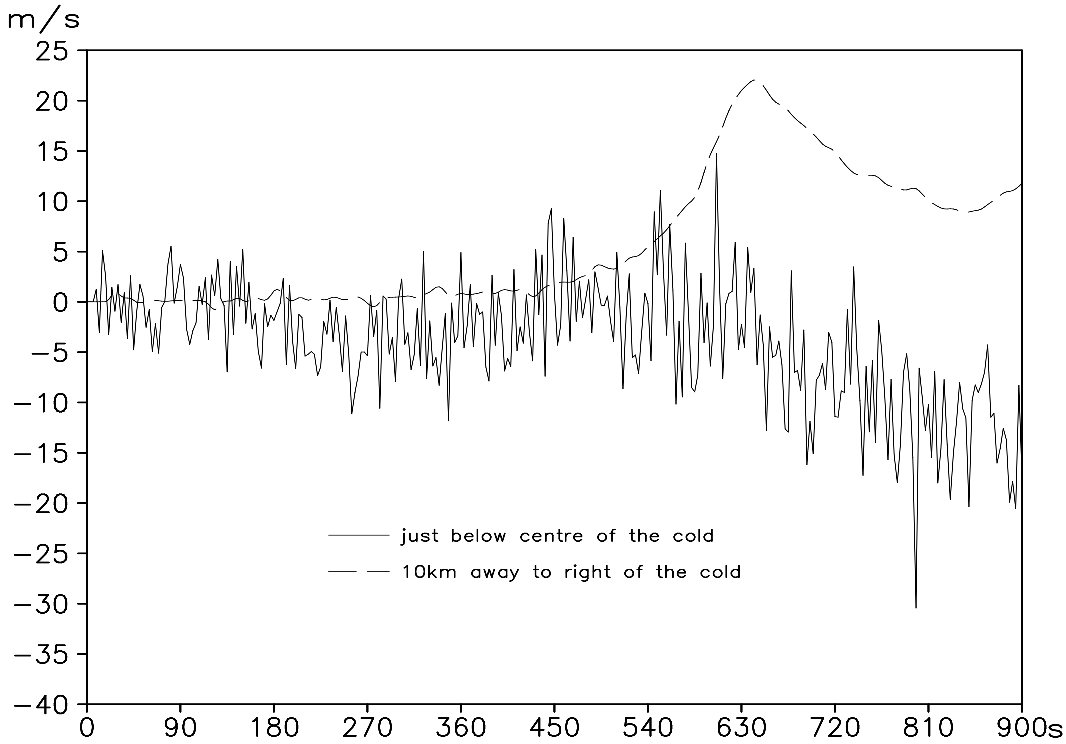

Fig.9. Surface horizontal wind change curve diagram of the density flow Test 1.

Surface horizontal wind at the cold surge center (solid line: $10^{-4}\mathrm{m \cdot s^{-1}}$), surface horizontal wind 10 km to the right of the cold surge (dashed line: $\mathrm{m \cdot s^{-1}}$), integrated for 900 s.

8 Gravity wave test

3D gravity wave test is performed to test the topographic perturbation caused gravity wave process of hydrostatic, non-hydrostatic dynamic core, and comparable results.

8.1 Initial value field

The initial value field of gravity wave test is also an equilibrium flow that satisfies hydrostatic equilibrium and proves to be horizontal motion quasi-geostrophic equilibrium.

The stable stratification constant frequency of buoyancy oscillation in the atmosphere N (take $\mathrm{N}^2 = 1.4 \times 10^{-4}$, N is also called Brunt-Väsälä frequency), because $\mathrm{N}^2 = -g \dfrac{\partial \ln \theta}{\partial z}$ (θ is the potential temperature), it has the following established relationship with the temperature lapse rate (equation (60)) (let T_0 be a constant):

$$\gamma = -\frac{\partial T}{\partial z} = \frac{\mathrm{N}^2}{g} T_0 + \frac{g}{C_p} \tag{73}$$

Combining the hydrostatic equilibrium equation, quasi-geostrophic equilibrium and the constant temperature lapse rate (equation (73)), the “solution” of the initial value field of $\hat{z}$ coordinates can be obtained (let

$$G = \frac{\gamma u_0}{g}(2\Omega r_0 + u_0)):$$

$$T(\lambda,\varphi,\hat{z}) = T_0 - \gamma(\frac{\Delta Z_s}{z_T}\hat{z} + z_s) - \frac{G}{2}\sin^2\varphi \tag{74}$$

$$p(\lambda,\varphi,\hat{z}) = p_0[\frac{T(\lambda,\varphi,\hat{z})}{T_0}]^{\frac{g}{R\gamma}} \tag{75}$$

In the above equation, take $p_0 = 1020$ hPa, $T_0 = 290.15$ K as the equatorial surface pressure and temperature, respectively, and take the initial value field $u = 8$ ms^{-1}, $v = \hat{w} = q = 0$, because $w = \hat{w}\frac{\Delta Z_s}{z_T} + w_s\frac{\Delta Z_{\hat{z}}}{z_T}$, then each $\hat{z}$ layer can be obtained $w = w_s\frac{\Delta Z_{\hat{z}}}{z_T}$ by diagnosis.

8.2 Bicubic surface "bell-shaped" terrain

Suppose the ideal "bell-shaped" terrain be:

$$h = \frac{H}{(1 + \frac{x^2}{L_x^2} + \frac{y^2}{L_y^2})^{\frac{3}{2}}} \tag{76}$$

H is the highest height of the central point of the terrain, x, y denote the east-west and north-south distances from the central part of the terrain, L_x, L_y denote the half-width of the terrain in the east-west and north-south directions, respectively, and take $L_x = 5\Delta x$, $L_y = 5\Delta y$.

The "bell-shaped" terrain is placed in the south-north center and western part along the west-east direction of the simulation area, and there is no terrain in the other areas, and the height field of the surface layer is fitted to the bicubic surface to form an overall "second-order derivative" bicubic surface terrain (Figure 10).

8.3 Simulation area and boundary

Simulation area 1 (Figure 10): horizontal resolution: 0.1°×0.1°, grid spacing: Δx≈Δy=11.12km, horizontal area (0:10°E, 5°S:5°N), a total of (0:100, −50:50) 10201 grid points. The 42-layer vertical stratification is carried out by converting the air pressure difference using the hydrostatic equilibrium equation (0:41) Δp = 25hPa (top layer Δp = 19hPa) to height difference Δz, atmospheric pressure layers: 1020, 995, 970, …, 45, 20, 1 (hPa), corresponding height layers: 0, 210, 422, … 15007, 16654, 19662 geopotential meter, and then converted to $\hat{z}$ coordinate stratification.

Simulation area 2: the horizontal resolution of 0.05°×0.05°, grid spacing Δx≈Δy=5.56km, horizontal area (0:5°E, 2.5°S:2.5°N), a total of (0:100, −50:50) 10201 grid points, vertical stratification is the same as simulation area 1.

Simulation area 3: the horizontal resolution of 0.01º×0.01º, grid spacing Δx≈Δy=1112 m, horizontal area (0:1 °E, 0.5 °S:0.5 °N), a total of (0:100, −50:50) 10201 grid points, vertical stratification is the same as simulation area 1.

The *x*-direction is the periodic cubic spline; the *y*-direction is the rigid boundary ($P^{y} \equiv 0$); the top and bottom layers in the *z*-direction: pressure field are both the hydrostatic equilibrium boundaries, while temperature, wind, displacement, and divergence fields are all the forward and backward difference boundaries.

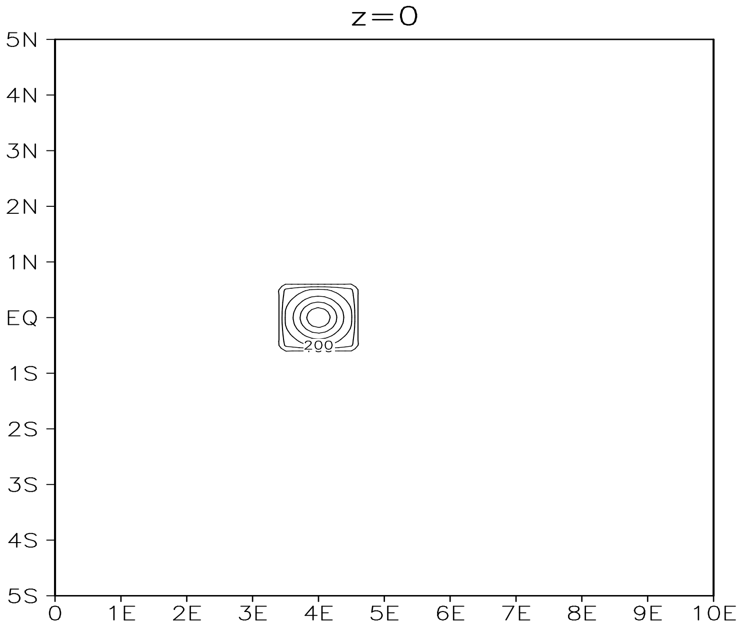

Fig. 10. Gravity wave test.

Simulation area 1 and the bell-shaped terrain (h: m, Δh: 100 m) for the gravity wave Test 1.

8.4 Gravity wave test analysis

①Test 1 (in the simulation area 1)

Non-hydrostatic dynamic core, the central height of terrain H = 600 m, its central point is (40,0) (Figure 10), $\Delta t = \delta t = 15\,\mathrm{s}$, integrated for 3h, (Test 1 shows: with stable atmospheric stratification and no water vapor evaporation and condensation precipitation, the no time separation is appropriated).

Test 1, if H = 0 m, which means that there is no terrain, becomes another “equilibrium flow test” in the limited area: when integrated for 3h, the pressure, temperature, and wind fields almost remain unaltered (figure omitted).

The u-v wind field ($\hat{z} = 210\,\mathrm{m}$): (0–3h integration, Figure 11), the horizontal airflow passes around or over mountain when meeting the terrain, divides into north and south branches on the windward slope, and after bypassing the terrain, converges into a flat airflow on the leeward slope (Figure 11 for 1h integration). But the test shows that the terrain forces the airflow to lift, making the general divergence field over the terrain, gradually forming a low pressure on the ground (Figure 12). The wind field adjusts to the pressure field, forming a gravity wave wind field with the leeward slope as the convergence center, “convergence-divergence-convergence-…” stationary wave propagating in all directions, with the leeward wave amplitude being most noticeable; (see Figure 11 for 2.5h integration), the gravity wave wind field propagation has reached the south and north boundaries, and crossed the east and west boundaries; however, since the periodic cubic spline is present, there are no East and West boundaries, so the gravity wave wind field becomes a “closed” annular wind tunnel flow.

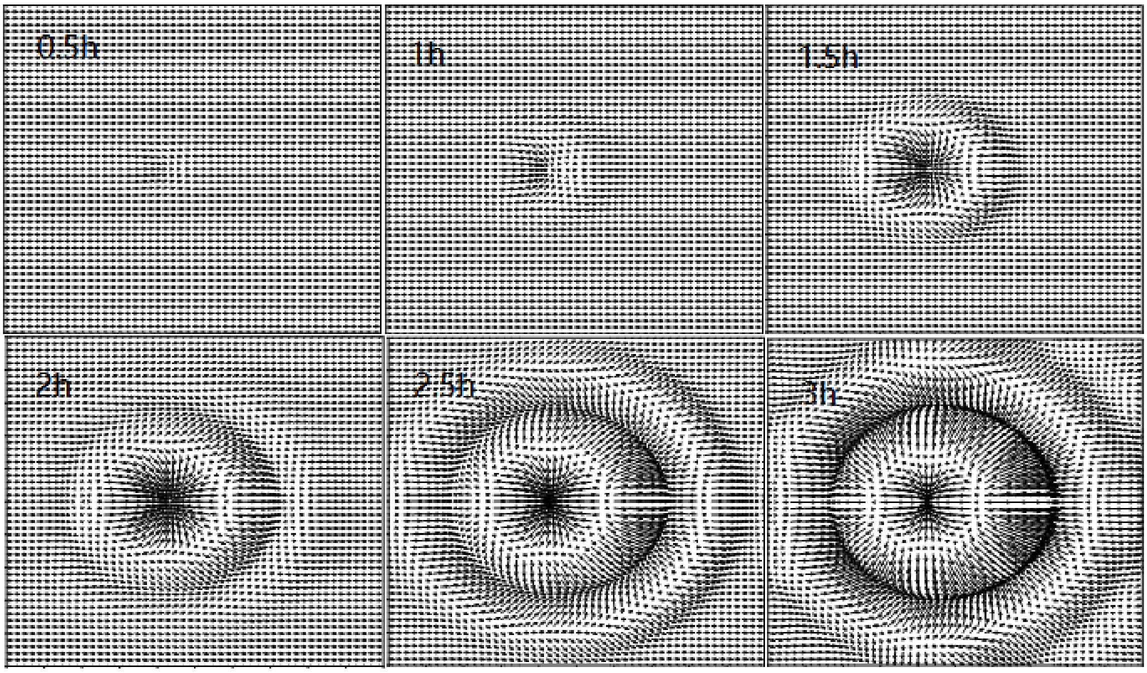

Fig. 11. Gravity wave test 1.

Simulated u-v field, 0.1º × 0.1º, $\Delta x \approx \Delta y \approx 11.12$ km, $\hat{z} = 210\,\mathrm{m}$, $\Delta t = \delta t = 15$ s, T = 0–3h.

Surface pressure field: from the initial value field of 949.90 hPa at the summit and 995.20 hPa at the windward and leeward slopes to 938.33 hPa at the summit with 2.5h integration, 1000.26 hPa at the windward slope, and 989.31hPa at the leeward slope (Figure 12①); it transforms into a gravity wave pressure field with the terrain acting as the low-pressure center, there the leeward slope has a relatively low pressure while the windward slope has relatively high pressure, a stationary wave propagating in all directions with the leeward wave amplitude being the most noticeable, and the gravity wave pressure field’s wavelength being calculable through diagnosis.

v-wind field ($\hat{z} = 2103\mathrm{m}$): (Figure 12②, 2.5h integration), presenting a v-field formed by the bypass flow, symmetric concerning the topography, revealing the standing wave-like pressure field and the horizontal gravity wave train. The perturbation has a closed wave number horizontal and vertical tilt structure.

(a) (b)

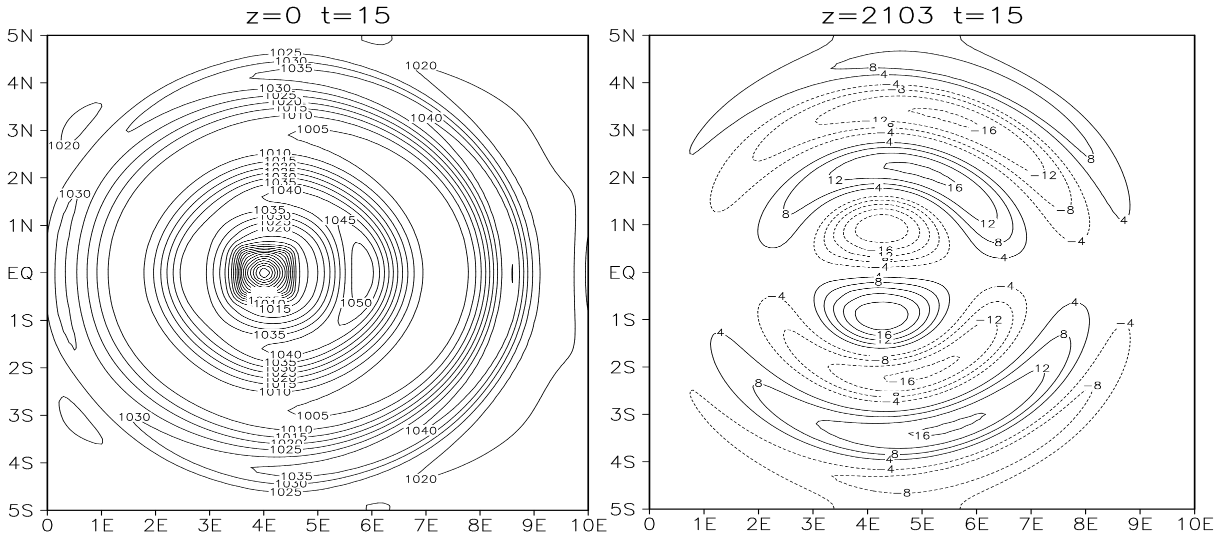

Fig. 12. Gravity wave Test 1.

(a) simulating surface pressure field, $\hat{z} = 0\,\mathrm{m}$, T = 2.5 h; (b) simulating the v field, $\hat{z} = 2103\mathrm{m}$, T=2.5 h

w-wind field: (see Figure 13, that is equatorial vertical cross-section) Figure 13①, 2.5h integration, shows the vertical structure of gravity wave propagation around the terrain, upwind and downwind, but the amplitude of the leeward wave is most noticeable on the downwind side. This motion wave train corresponds to the topographically disturbed standing wave type pressure field formed by the “fully compressible” equilibrium flow crossing the mountain for a long time.

Test 1 shows that the “horizontal hydrostatic, but vertical non-hydrostatic” dynamic core can simulate the terrain gravity wave pressure, temperature, and u-v-w wind field. They differ in time-space propagation, and intensity of the simulated terrain gravity waves, and have significantly different mountain front vertical velocities when compared to the w-wind field simulation utilizing the vertical hydrostatic dynamic core (Figure 13②, 2.5h integration).

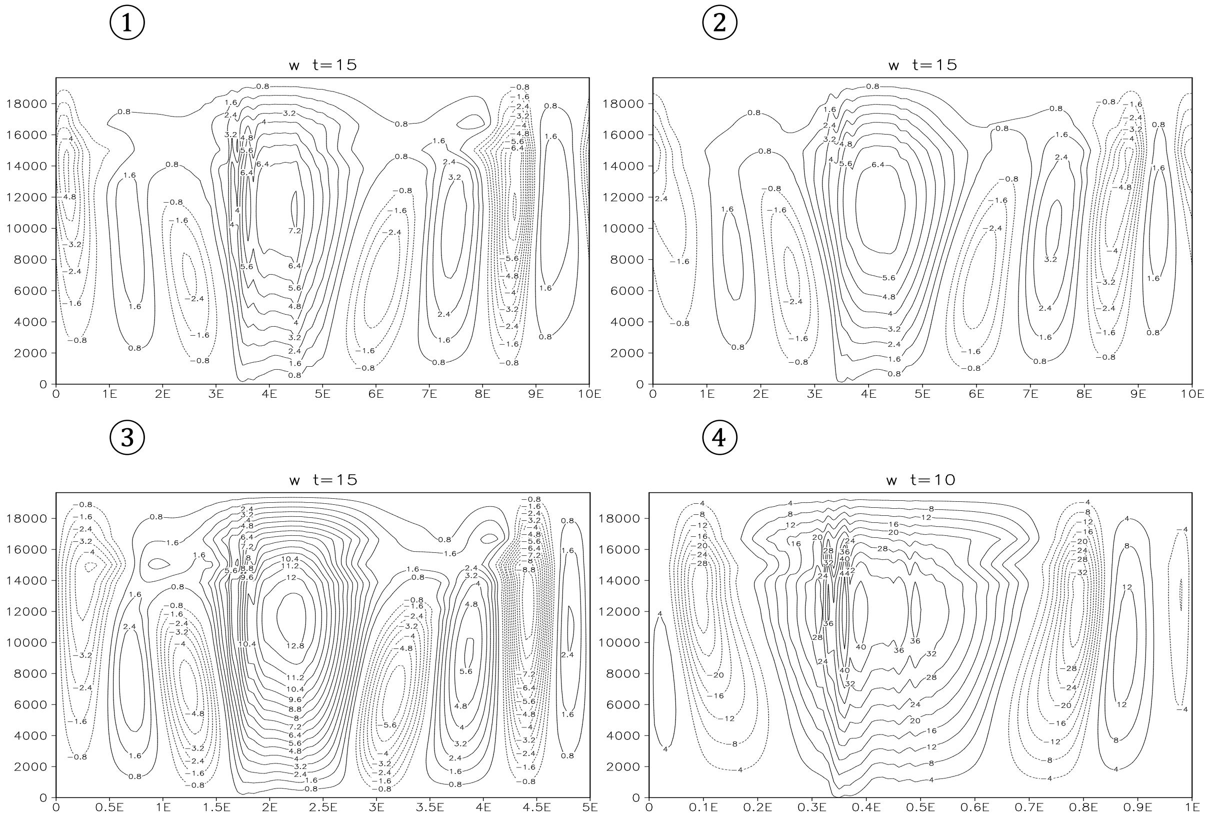

Fig. 13. Gravity wave Test 1, Test 2, and Test 1.

①Gravity wave Test 1, simulating w-field, equatorial $x-\hat{z}$ profile, of$0.1^\circ \times 0.1^\circ$, $\Delta x \approx \Delta y \approx 11.12$km, $\Delta t = \delta t = 15$s, T = 2.5h; ②is the same as ① but for the hydrostatic dynamic core; ③gravity wave Test 2, simulating w-field, equatorial $x-\hat{z}$ profile, but of $0.05^\circ \times 0.05^\circ$, $\Delta x \approx \Delta y \approx 5.56$ km, $\Delta t = \delta t = 6$s, T = 90 min; ④gravity wave Test 3, simulating w-field, equatorial $x-\hat{z}$ profile, but of $0.01^\circ \times 0.01^\circ$, $\Delta x \approx \Delta y \approx 1112$ m, $\Delta t = \delta t = 1$s, T = 20 min.

②Test 2 (in the simulation area 2)

Non-hydrostatic dynamic core, the central height of terrain H=200m, central point (80,0), $\Delta t = \delta t = 6\,\mathrm{s}$, integrated for 108 min. Test 2 has a half grid, four times smaller terrain extent and twice as high spatial resolution as Test 1.

u-v wind field (figure omitted): similar to Test 1, but integrated for 96 min, the gravity wave wind field extends to and crosses the east and west boundaries as well as the south and north boundaries.

w-wind field: Figure 13③, 90 min integration, demonstrates the gravity wave train and the vertical velocity distribution.

③Test 3 (in the simulation area 3)

Non-hydrostatic dynamic core, the central height of terrain H=100m, central point (80,0), $\Delta t = \delta t = 1\,\mathrm{s}$, integrated for 30 min. Test 3 has a 10 times smaller grid (100 times smaller terrain extent) and 10 times higher spatial resolution than Test 1.

u-v wind field (figure omitted): similar to Test 1, the gravity wave wind field crosses the east and west borders and propagates to the south and north boundaries despite only being integrated for 26 minutes.

w-wind field: Figure 13④, 20 min integration, demonstrates the gravity wave train and the vertical velocity distribution.

9 Conclusion and discussion

(1) In spherical coordinates, the “thin atmosphere” atmospheric motion equation, including the north and south poles, is given.

(2) The general space-time discretization 1st-order and 2nd-order accuracy forecast equations in the spline format are provided.

(3) There is 3D divergence separation: 3D divergence = hydrostatic horizontal divergence + non-hydrostatic vertical divergence, which serves as the physical foundation for the time-split integration scheme. The non-hydrostatic dynamic core is completed by using long steps for hydrostatic horizontal advection and short steps for non-hydrostatic vertical convection.

(4) The methods for calculating bicubic surface terrain and terrain-following vertical coordinates and horizontal pressure gradient force in spline format, the time-varying reference atmosphere and vertical pressure gradient force calculation method in spline format, and the space-time discretization 3D “displacement” divergence in spline format. There are two types of divergence, namely, hydrostatic horizontal “displacement” divergence and non-hydrostatic vertical “displacement” divergence.

(5) The vector discrete decomposition method is given: based on the correspondence between the “upstream point of spherical coordinates - 3D displacement of Cartesian coordinates - spherical coordinate forecast point” 3D wind and displacement field are solved using implicit iteration based on the correspondence between Cartesian coordinates and spherical coordinates.

(6) The forecast equation of a “non-hydrostatic fully compressible” pressure-temperature field is provided, but with a time step of only 0.1s.

(7) The physical concept of “half-wave oscillation” is proposed. Under the action of vertical pressure gradient force, the layers of the air column shift to hydrostatic equilibrium (the oscillating pendulum reaches the equilibrium point) within the one-time step, and the corresponding acoustic calculation scheme. Calculating the vertical displacement of each layer of non-hydrostatic vertical motion “half-wave oscillation” and the “full compressible” pressure and temperature field by implicit iteration not only preserves the physical mechanism of compression wave vertical motion “acoustic + gravity wave,” but also effectively avoids acoustic propagation.

(8) With a time step of 10s, a quasi-Lagrangian time-split integration scheme is given. Hydrostatic horizontal advection + “half-wave oscillation” non-hydrostatic vertical convection, while maintaining atmospheric mass conservation in the model.

(9) Mathematically, the spline format is a second-order derivable format, and its linear principal part is the second-order central difference. It is simple to demonstrate that the second-order central difference, compared to the first-order central difference, has half the spatial truncation error, the phase velocity of propagation, and the group velocity of dispersion errors. The ideal field tests show that the spline format describes the fluctuation phase velocity and phase without error, but there is amplitude decay and energy dispersion error. The second-order spatial residual of the cubic spline and the upstream point path’s truncation calculation error, for the path does not reach the exact trajectory, are the two causes of inaccuracy in the spline format.

The equilibrium flow test demonstrates that the spline format and the linear format can be “compatible”, but the spectrum is not compatible with the linear format, such as the Gibbs phenomenon.

The R-H wave test demonstrates that the spline format’s spatial resolution only demonstrates identification, and that fidelity can only be ensured when the spatial and temporal resolutions are superimposed. The spline format error also shows amplitude decay as the spatial and temporal resolutions increase. The pressure field tends to become “round” as a result of the amplitude decay in erroneous error, which possesses spherical symmetry. It should be noted that the earth’s rotation and atmospheric geostrophic motion are spherically symmetric, and the spline format forecasted waves becoming “round” and linear motion is consistent with the wave energy dispersion, When the variable field is becoming “round,” a new equilibrium flow is formed due to momentum dissipation, the “round” ground rotation motion, and this amplitude decay error, which is convergent, monotonic, and bounded.

(10) Longitude-latitude grid (A-grid) - quasi-uniform longitude-latitude grid (B-grid) spline format transformation: the scalar and vector fields, such as pressure, temperature, humidity, wind, and generalized Newtonian force fields, are fitted to a bicubic surface on the A-grid, and on B-grid points, only advection forecasts are made, and the upstream point’s horizontal motion routes and variable values are determined via implicit iteration, and all A-grid points are given “forecast values” using cubic spline interpolation of the forecast variables. The spline format interpolation can solve the classical problems of the over-dense grid in the polar region and singularity at the poles.

The cross-polar flow test confirms that the geostrophic advection and the A-B longitude-latitude grid spline format transformation can cross the polar region and the pole correctly, and it demonstrates that the north and south poles’ horizontal motion equations are accurate.

In the R-H wave test, the “round” result of the A-B longitude-latitude grid spline format transformation when integrated for 300 d is contrasted with the “partially round” result of the Gaussian grid spectral transformation when integrated for 80 d, because the spectral expansion for wind field is undefined at the poles and asymmetric concerning the poles.

(11) In the density flow test, the density flow is “acoustic + gravity wave”, it is safe to assume that the spline format will outperform/not be inferior to the linear format. This is because it simulates the highly nonlinear, fine-scale, transient “pressure-temperature-wind” field characteristics of the density flow, like a downburst, and because the simulation results are similar to the benchmark linear format reference results. The density flow test uses “non-hydrostatic full compressible” 3D divergence to act on and predict the pressure and temperature field directly, so there is sound wave propagation, and the time step is only 0.1 s.

(12) The gravity wave test simulated the equilibrium flow and terrain interaction, forming cross-mountain airflow terrain gravity wave pressure and temperature fields, and wave horizontal and vertical propagation. It adopts the time-split integration scheme, and the time step can be 10 s. The time separation is not needed under stable stratification conditions, i.e., the time separation can be used only for the physical process of “cumulus convection parameterization and precipitation”. However, the test results of this paper and those of Yang et al. (2008), who completed the gravity wave tests for the GRAPES model non-hydrostatic fully compressible dynamic core, summarized that the results of the gravity wave tests for other non-hydrostatic fully compressible dynamic cores, differ noticeably. One possible explanation is the stepped topography when the linear format is used, while we introduced the “bicubic surface” second-order derivative terrain.

The gravity wave test demonstrated the “hydrostatic/non- hydrostatic dynamic core with space-time second-order precision” preliminarily: quasi-Lagrangian time-split integration scheme + bicubic surface terrain-following vertical coordinates + “half-wave oscillation” acoustic wave calculation scheme + “spherical coordinate - rectangular coordinate - spherical coordinate” vector discretization method.

(13) The ideal field tests show that the stability of the spline format depends on proper smoothing of the variable field, and smoothing is also a source of error. If it is always with the spline format to match wind field to the second-order derivable, that is mathematically incompatible because the wind field is frequently zero-order continuous: shear lines commonly emerge on wind fields, such as cold / warm fronts and frontal cyclones.

Future research will focus on how to combine different functions or step-down functions of variable fields, or to smooth a lot of points / single point of variable fields; especially in the case of wind fields, based on the spline fit’s curvatures judgment, as well as how to easily find the smooth domain/point a second-order derivable patch to get rid of redundant inflection points, discontinuous cusps or wraps (that is like that "sprays" in river tend to be smooth), are to be studied in the future.

(14) The ideal field tests confirm the viability, consistency with the linear format, second-order accuracy, and stability of the spline format in computing the “three-time motion” path of the upstream point. For the spline format’s hydrostatic / non-hydrostatic dynamic core, physical process parameterization schemes and synoptic verification are to be introduced to ultimately develop into a globally unified, multiple nested grid mesh numerical model prediction system.

Code availability. The spline model code developed in this article can be downloaded for free from https://orcid.org/0000-0001-6491-7051.

Data availability. All data can be accessed by contacting the corresponding author Xuzan Gu (guxuzan@163.com).

Author contributions. XG developed the numerical dynamic core to calculate these exact tests. XG developed the code. XG performed the computations. XG, ZW and YG jointly analysed the calculation results and wrote the paper together.

Competing interests. The contact author has declared that neither they nor their co-authors have any competing interests.

Disclaimer.

Financial support. This research has been supported by the National Natural Science Foundation of China (grant no. 42075143).

REFERENCES

Bates, J. R., Semazzi, F. H. M., Higgins, R. W., et al., 1990: Integration of the shallow water equations on the sphere using a vector semi-Lagrangian scheme with a multigrid solver. *Mon. Wea. Rev.*, **118**, 615-617, https://doi.org/10.1175/1520-0493(1990)118%3C1615:IOTSWE%3E2.0. CO;2

Benacchio, T., Neill, W. P. O., and Klein, R., 2014: A blended soundproof-to-compressible numerical model for small- to mesoscale atmospheric dynamics. *Mon. Wea. Rev.*, **142**, 4416-4438, https://doi.org/ 10.1175/MWR-D-13-00384.1

Daley, R. W., 1988: The normal modes of the spherical non-hydrostatic equations with applications to the filtering of acoustic modes. ***Tellus***, **40A**, 96-106, https://doi.org/10.1111/j.1600-0870.1988. tb00409.x

Dudhia, J., 1993: A non-hydrostatic version of the Penn State-NCAR mesoscale model: validation tests and simulation of an Atlantic cyclone and cold front. *Mon. Wea. Rev.*, **121**, 1493-1513, https://doi.org/ 10.1175/15200493(1993)121%3C1493: ANVOTP%3E2.0.CO;2

Durran, D. R., and Blossey, P. N., 2012: Implicit–explicit multistep methods for fast-wave–slow-wave problems. *Mon. Wea. Rev.*, **140**: 1307–1325, https://doi.org/10.1175/MWR-D-11-00088.1

Fergusion, J. C., 1964: Multivariable curve interpolation. *J. ACM*,**2**, 221-228.

Gavrilov, N. M., Kshevetskii, S. P., and Koval, A. V., 2015: Verifications of the high-resolution numerical model and polarization relations of atmospheric acoustic-gravity waves, Geosci. Model Dev., 8, 1831–1838, https://doi.org/10.5194/gmd-8-1831-2015.

Gu, X. Z., 2011: A new quasi-Lagrangian time integration scheme with the interpolation of fitting bicubic surface. *Acta Meteorologica Sinica*. **3**, 440-446, https://doi: 10.11676/qxxb2011.038 (in Chinese)

___, Tang, Y. L., 2013: Bicubic-Surface topography computing the horizontal pressure gradient force in the numerical wenther prediction model. *Plateau Meteorology*. **32**, 88-96, http://doi:1000-0534. 2012.00010 (in Chinese)

Günther Zängl, 2012: Extending the numerical stability limit of terrain-following coordinate models over steep slopes. *Mon. Wea. Rev.*, **140**, 3722-3733, https://doi.org/10.1175/mwr-d-12-00049.1

Jacobs, C. T. and Piggott, M. D., 2015: Firedrake-Fluids v0.1: numerical modelling of shallow water flows using an automated solution framework, Geosci. Model Dev., 8, 533–547, https://doi.org/10.5194/ gmd-8-533-2015.

Layton, A. T., 2002: Cubic spline collocation method for the shallow water equations on the sphere, *J. Comput. Phys.*, **179**, 578-592,doi:10.1006/jcph.2002.7075

Li, J., Zhang, Q., and Chen, T., 2022: ISWFoam: a numerical model for internal solitary wave simulation in continuously stratified fluids, Geosci. Model Dev., 15, 105–127, https://doi.org/10.5194/gmd-15-105-2022.

Liu, Y., Chen, D. H., Hu, J. L., et al., 2011: An impact study of the orographic effective scales for GRAPES_meso model with idealized numerical simulations. *Tropical Meteorology Journal*. **1**, 53-62, (in Chinese)

Nunalee, C. G., Horváth, Á., and Basu, S., 2015: High-resolution numerical modeling of mesoscale island wakes and sensitivity to static topographic relief data, Geosci. Model Dev., 8, 2645–2653, https://doi.org/10.5194/gmd-8-2645-2015.

Pinty, J. P., Benoit, R., Richard E., et al., 1995: Simple tests of a semi-implicit semi-Lagrangian model on 2D mountain wave problems. *Mon. Wea. Rev.*, **123**, 3042-3058, https://doi.org/10.1175/1520-0493 (1995)123%3C3042:STOASI%3E2.0.CO;2

Qian, J. H., Semazzi, F. H. M., and Scroggs, J. S., 1998: A global nonhydrostatic semi- Lagrangian atmospheric model with orography. *Mon. Wea. Rev.*, **126:** 747-771, https://doi:10.1175/ 1520-0493(1998)126%3C0747:AGNSLA%3E2.0.CO;2

Robert, A., Yee, T. L., Ritchie, H., 1985: Semi- Lagrangian and semi-implicit numerical integration scheme for multilevel atmospheric models. *Mon. Wea. Rev.*, **113**, 388-394, https://doi.org/10.1175/1520-0493(1985)113%3C0388:ASLASI%3E2.0.CO;2

Saito, K., Doms, G., Schaetter, U., et al., 1998: 3-D mountain waves by the lokal-modell of dwd and the mri-mesoscale nonhydrostatic model. *Pap. Met. Geophys*, **49**: 7-19.

Smith, R. B., 1980: Linear theory of stratified hydrostatic flow past an isolated mountain. *Tellus*, **32**, 348-364,doi:10.1111/j.2153-3490.1980.tb00962.x

Straka, J. M., Wilhelmson, R. B., Wicker, L. J., et al., 1993: Numerical solutions of a non-linear density current: a benchmark solution and com-parisons. *Int J Numer Methods Fluids*, **17**, 1-22

Su, Y., Shen, X. S., Chen, Z. T., et al., 2018: A study on the three-dimensional reference atmosphere in GRAPES_GFS: Theoretical design and ideal test. *Acta Meteorologica Sinica*,**76**:241-254, doi: 10.11676/qxxb2017.097 (in Chinese)

Xu, Q., Xue, M., and Droegemeer, K. K., 1996: Numerical simulations of density currents in sheared environments within a vertically confined channel. *J. Atmos. Sci.*, 53, 770-786, https://doi.org/10.1175/1520-0469(1996)053%3C0770:NSODCI% 3E2.0.CO;2

Xue, M., Droegemeier, K. K., and Wong, V., 2000: The advanced regional prediction system (ARPS)-A Multi-scale nonhydrostatic atmospheric simulation and prediction model, Part I: Model dynamics and verification. *Met. Atmos. Phys.*, **75**: 161-193, https://doi:10.1007/s007030070003

___, Xu, Q. and Droegemeier, K. K., 1997: A theoretical and numerical study of density currents in non-constant shear flows. *J. Atmos. Sci.*, **54**: 1998-2019, https://doi.org/10.1175/1520-0469(1997)054% 3C1998:ATANSO%3E2.0.CO;2

Yang, X. S., Chen, J. B., and Hu J. L., et al., 2007: Polar discretization of grapes global non-hydrostatic semi-implicit semi-lagrangian model. *Sci China Ser D-Earth Sci*, **50**: 1885-1891.

___, Hu, J. L., Chen, D. H., et al., 2008: Verification of a unified global and regional numerical weather prediction model dynamic core. *Chinese Science Bulletin*, **53,**1-7.

Zuo, R.T., Zhang, M., Zhang, D. L., et al., 2004: Designing and climatic numerical modeling of 21-Level AGCM(IAP AGCM-Ⅲ) Part Ⅰ:Dynamical Framework. *J. Atmos. Sci.*, **28**: 659-674, https://doi: 10.3878/j.issn.1006-9895.2004.05.02 (in Chinese)